CERN – EUROPEAN ORGANIZATION FOR NUCLEAR RESEARCH

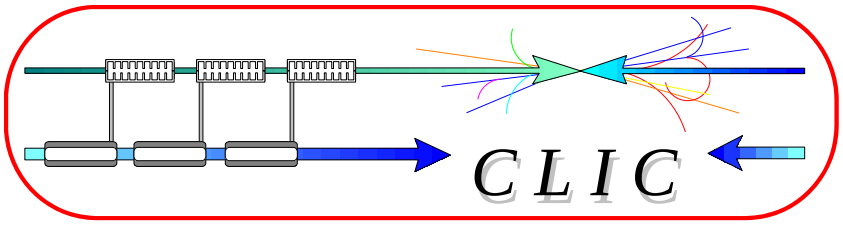

CLIC-Note-769

DESIGN AND CONSTRUCTION OF A BEAM POSITION MONITOR PROTOTYPE FOR THE TEST BEAM LINE OF THE CTF3

J J Garcia Garrigos
Universitat Politecnica de Valencia, Spain

CERN-OPEN-2009-002
30/09/2008

Abstract

A prototype of Beam Position Monitor (BPM) for the Test Beam Line (TBL) of the 3*rd* CLIC Test Facility (CTF3) at CERN has been designed and constructed at IFIC in collaboration with the CERN CTF3 team. The design is a scaled version of the BPMs of the CTF3 linac. The design goals are a resolution of 5 μm, an overall precision of 50 μm, in a circular vacuum chamber of 24 mm, in a frequency bandwidth between 10 kHz and 100MHz.The BPMis an inductive type BPM. Beam positions are derived from the image current created by a high frequency electron bunch beam into four electrodes surrounding the vacuum chamber. In this work we describe the mechanical design and construction, the description of the associated electronics together with the first calibration measurements performed in a wire test bench at CERN.

Geneva, Switzerland
(3 February 2009)

Universidad Politécnica de Valencia
DEPARTAMENTO DE INGENIERÍA ELECTRÓNICA

UNIVERSITAT
POLITÈCNICA
DE VALÈNCIA

Design and Construction of a Beam Position Monitor Prototype for the Test Beam Line of the CTF3

TRABAJO DE INVESTIGACIÓN

Juan José García Garrigós

Septiembre de 2008

Departamento de Ingeniería Electrónica
Universidad Politécnica De Valencia

UNIVERSIDAD POLITECNICA DE VALENCIA

Dr. Angeles Faus Golfe, Científico Titular del CSIC y
Dr. Angel Sebastiá Cortés, Catedrático de la Universidad Politécnica de Valencia

CERTIFICAN:

Que la presente memoria, *Design and Construction of a Beam Position Monitor Prototype for the Test Beam Line of the CTF3*, ha sido realizada en la Unidad de Física Experimental del Instituto de Física Corpuscular bajo nuestra dirección y supervisión, por D. Juan José García Garrigós y constituye su trabajo de investigación.

Y para que conste, en cumplimiento de la legislación vigente, firmamos el presente Certificado en Valencia a 6 de Octubre de 2008.

Fdo. Dr. Angeles Faus Golfe

Fdo. Dr. Angel Sebastiá Cortés

Acknowledgments

I would like to express my gratitude to IFIC —*Instituto de Física Corpuscular, CSIC-Universidad de Valencia*— for giving me the opportunity to realize this work in the field of beam instrumentation for particle accelerators. Jointly, thanks to the CTF3 —*CLIC Test Facility 3*— collaboration from CERN —*European Organization for Nuclear Research*— for helping us with such a challenging task of constructing the beam position monitor prototypes.

I am sincerely grateful to Dr. Angeles Faus Golfe, not only my supervisor at IFIC but, what I consider, a mentor for me, with her always encouraging support and leadership, also to my supervisor at the DIE-UPV —*Departamento de Ingeniería Electrónica-Universidad Politécnica de Valencia*— Dr. Angel Sebastiá Cortés for his kind advices and constant support.

I truly want to thank to Dr. Gabriel Montoro from the UPC —*Universidad Politécnica de Cataluña*— collaboration to develop the BPS external amplifier; for his strong and close commitment, and lots of fruitful conversations (even those about far-west movies and conspiracy theories), during the test stays at CERN labs. And, Dr. Benito Gimeno from the *Universidad de Valencia* for his experienced help in the understanding of the image current electromagnetic effects.

Also thanks to Dr. Steffen Döebert the project-leader of the TBL —*Test Beam Line*— in the CTF3, for trusting in our work and for his helpful advices, and to our direct collaborators, Lars Søby and Franck Guillot for their guiding advices, helping us at every moment in the lab, and for their hospitality (thanks for the good coffees).

Many thanks to the people directly involved in this project at IFIC, José Vicente Civera (Mechanical Unit) for the complex BPS prototype mechanical design and dedication to this work, Jorge Nácher (Electronic Unit) for making such cool PCBs as many times as I needed, César Blanch (Mechanical Unit) for the nice sketch of our future BPS testbench and his willingness; without their experience and help this work would have not been possible.

I must acknowledge the participation of our industry partners, *G&P Vacuum Projects* and *Talleres Lemar* for their great job in the BPS prototypes manufacturing.

I also would like to extend my gratitude to all my colleagues at IFIC for such a kind fellowship, and specially to María del Carmen Alabau for sharing the office with me and being always ready to help me with a smile.

Finally, special and very well-deserved thanks to my wife, María José, —
she is everything I need that I never knew I wanted;
she is everything I want that I never knew I needed
(The Fray, How to Save a Life)—.

Summary

A prototype of Beam Position Monitor (BPM) for the Test Beam Line (TBL) of the 3^{rd} CLIC Test Facility (CTF3) at CERN has been designed and constructed at IFIC in collaboration with the CERN CTF3 team. The design is a scaled version of the BPMs of the CTF3 linac. The design goals are a resolution of 5 μm, an overall precision of 50 μm, in a circular vacuum chamber of 24 mm, in a frequency bandwidth between 10 kHz and 100 MHz.The BPM is an inductive type BPM. Beam positions are derived from the image current created by a high frequency electron bunch beam into four electrodes surrounding the vacuum chamber. In this work we describe the mechanical design and construction, the description of the associated electronics together with the first calibration measurements performed in a wire test bench at CERN.

Contents

Chapter 1

The CLIC Test Facility 3 project at CERN

1.1 The Compact Linear Collider (CLIC)

. The latest and foremost accelerator at CERN the LHC (Large Hadron Collider), is set to provide a rich programme of physics at a new high-energy frontier over the coming years. From September 2008 onwards, the LHC will probe the new *terascale* energy region. It should above all confirm or refute the existence of the Higgs boson to complete the Standard Model (see figure 1.1), explaining how some particles get its mass through the so called Higgs mechanism. The LHC experiments will also explore the possibilities for physics beyond the Standard Model, such as supersymmetry, extra dimensions and new gauge bosons. The discovery potential is huge and will set the direction for possible future high-energy colliders. Nevertheless, particle physics community worldwide have reached a consensus that the results from the LHC will need to be complemented by experiments at an electron-positron collider operating in the tera-electron-volt energy range.

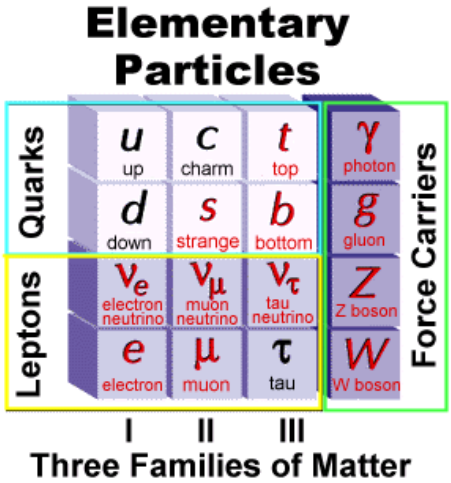

Figure 1.1: Elementary particle families of the Standard Model which describes all the fundamental forces of the nature, the electromagnetic, nuclear and weak forces; except the gravitation force, with the predicted graviton as its carrier.

The highest centre-of-mass energy in electron-positron collisions so far, 209 GeV, was reached at LEP (Large Electron-Positron collider) at CERN. In a circular collider, such as LEP, the circulating particles emit synchrotron radiation, and the energy lost in this way needs to be replaced by a powerful radio-frequency (RF) acceleration system. In LEP, for example, each beam lost about 3% of its energy on each turn. The biggest superconducting RF system built so far, which provided a total of 3640 MV per revolution, was just enough to keep the beam in LEP at its nominal energy. Moreover, the energy loss by synchrotron radiation increases with the fourth power of the energy of the circulating beam. So it is clear that a storage ring is not an option for an electron-positron collider operating at an energy significantly above that of LEP, as the amount of RF power required to keep the beam circulating becomes prohibitive.

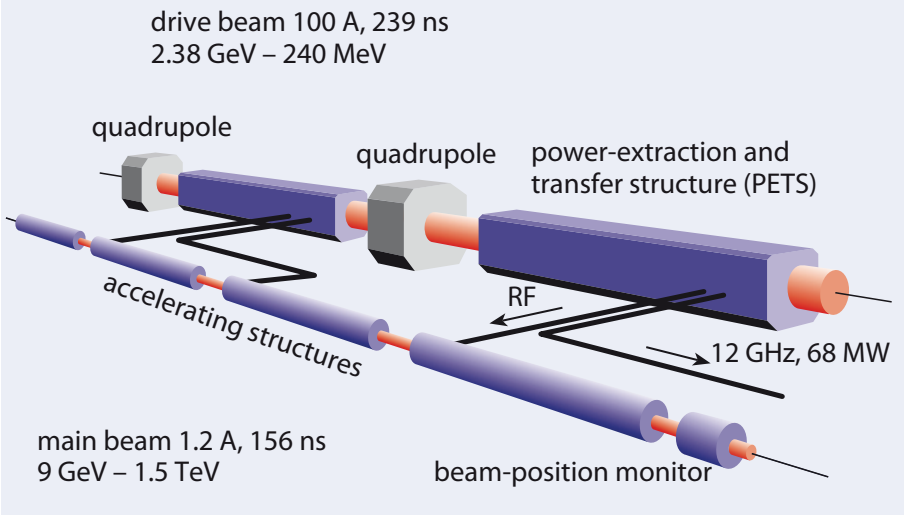

Figure 1.2: The CLIC two-beam acceleration scheme for a center-of-mass collision energy of 3 TeV, with the main beam accelerated by the RF power provided from the lower-energy but high-current drive beam (not to scale).

Linear colliders are therefore the only option for realizing electron-positron collisions at tera-electron-volt energies, avoiding synchrotron radiation losses. The basic principle here is simple: two linear accelerators face each other, one accelerating electrons (e^-), the other positrons (e^+), so that the two beams of particles can collide head on. This scheme has certain inherent features that strongly influence the design. First, the linacs have to accelerate the particles in one single pass. This requires high electric fields for acceleration, so as to keep the length of the collider within reasonable limits; such high fields can be achieved only in pulsed operation. Secondly, after acceleration, the two beams collide only once. In a circular machine the counter-rotating beams collide with a high repetition frequency, in the case of LEP at 44 kHz. A linear collider by contrast would have a repetition frequency of typically 5–100 Hz. This means that the rate of collisions events, or luminosity, necessary for the particle physics experiments can be reached only with very small beam dimensions at the interaction point and with the highest possible number of charged particles in a single bunch. As luminosity is proportional to beam power, the overall wall-plug to acceleration efficiency is of paramount importance.

The ILC collaboration [1] is studying a machine with a centre-of-mass energy of

500 GeV and a possible future upgrade to 1 TeV. This study is based on an RF system using superconducting cavities for acceleration, with a nominal accelerating field of 31.5 MV/m and a total length of 31 km for a colliding-beam energy of 500 GeV. The RF superconducting cavities system is a well-known and proven technology which represents the state-of-the-art in acceleration technology.

At the same time, the Compact Linear Collider (CLIC) [2] study is aiming at a nominal energy of 3 TeV, and foresees building CLIC in stages, starting at the lowest energy required by the physics, with successive energy upgrades that can potentially reach about five times the energy of the ILC. The CLIC scheme is based on normal conducting travelling-wave accelerating structures, operating at a frequency of 12 GHz and with very high electric fields of 100 MV/m to keep the total length to about 48 km for a colliding-beam energy of 3 TeV. Such high fields require high peak power and hence a novel power source. An innovative two-beam system, in which another beam, the drive beam, supplies energy to the main accelerating beam.

The RF power peak required to reach the electric fields of 100 MV/m amounts to about 275 MW per active meter of accelerating structure. With an active accelerator length for both linacs of 42 km out of the 48 km total length of CLIC, the use of individual RF power sources, such as klystrons, to provide such a high peak power is not really possible. Instead, the key innovative idea underlying CLIC is a two-beam scheme to produce and distribute the high peak RF-power. In this system, two beams run parallel to each other: the main beam, to be accelerated, and the drive beam to provide the RF power for the accelerating structures (see figure 1.2).

To transfer the energy to the main beam, the drive beam passes through novel Power Extraction and Transfer Structures (PETS) shown in the figure 1.2, where it excites strong electromagnetic oscillations, i.e. the beam loses its kinetic energy to electromagnetic energy. Thus, as the beam is decelerated, the RF energy is extracted from the PETS and sent via waveguides to the accelerating structures in the parallel main beam. The PETS are travelling wave structures like the accelerating structures for the main beam, but with different parameters.

The proposed CLIC layout is presented in the figure 1.3, where we can differentiate the main sections. In the center region are the two main beam linacs facing each other to boost electrons, from the left side, and positrons, from the right side, toward collision. The particle detectors will be installed in the interaction point (IP), where the collisions take place, but just before two sophisticated beam delivery systems (BDS), one for each beam line, will focus the beam down to dimensions of 1 nm rms size in the vertical plane and 40 nm horizontally, in order to achieve the luminosity that the experiments demand. Running in parallel to each main linacs, there are the two decelerator lines, to extract the RF power from the drive beams through the PETS, and then transfer it to the main beams for accelerating them. In the top of the layout it can be seen the two-folded drive beam generation system which consists in two drive beam linacs fed by klystrons, followed by a sequence of three rings for each linac: a delay loop and two combiner rings (CR); leading to the required drive beam features of average beam current (100 A), energy (2.38 GeV) and bunches spaced by 2.5 cm (12 GHz) in bursts of 239 ns long. By the other hand, the main beams will also attain the suited features due to the main beam injection system where the electron and positron beams will come from their respective injectors, at 2.4 GeV, and finally accelerated to 9 GeV by the booster linac before entering in the main linacs.

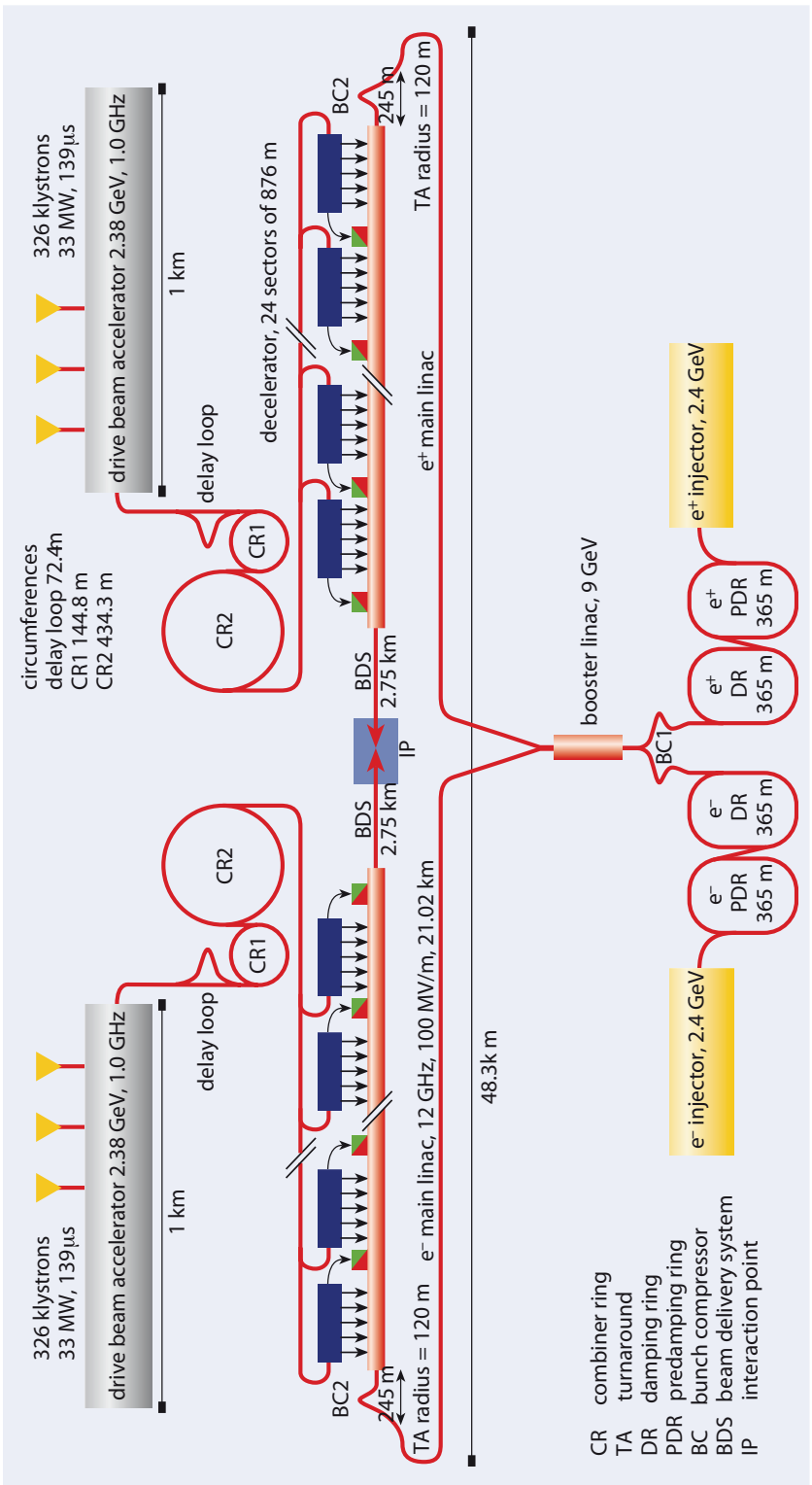

Figure 1.3: The CLIC layout, showing two-beam acceleration scheme and its dimensions (central part), the various components of the main beam injection system (lower side) and the drive beam generation system (upper side).

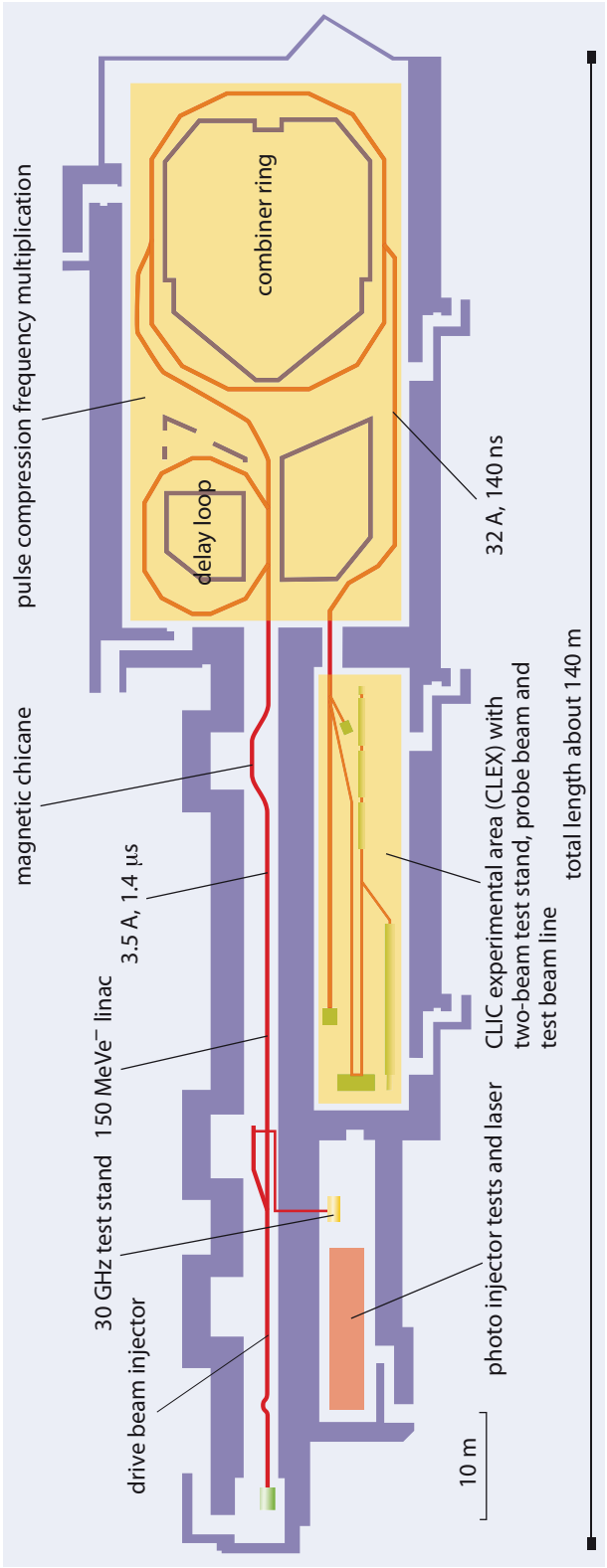

Figure 1.4: Diagram of the CLIC test facility (CTF3), with 150 MeV linac, delay loop and combiner ring, together with the experimental area, CLEX.

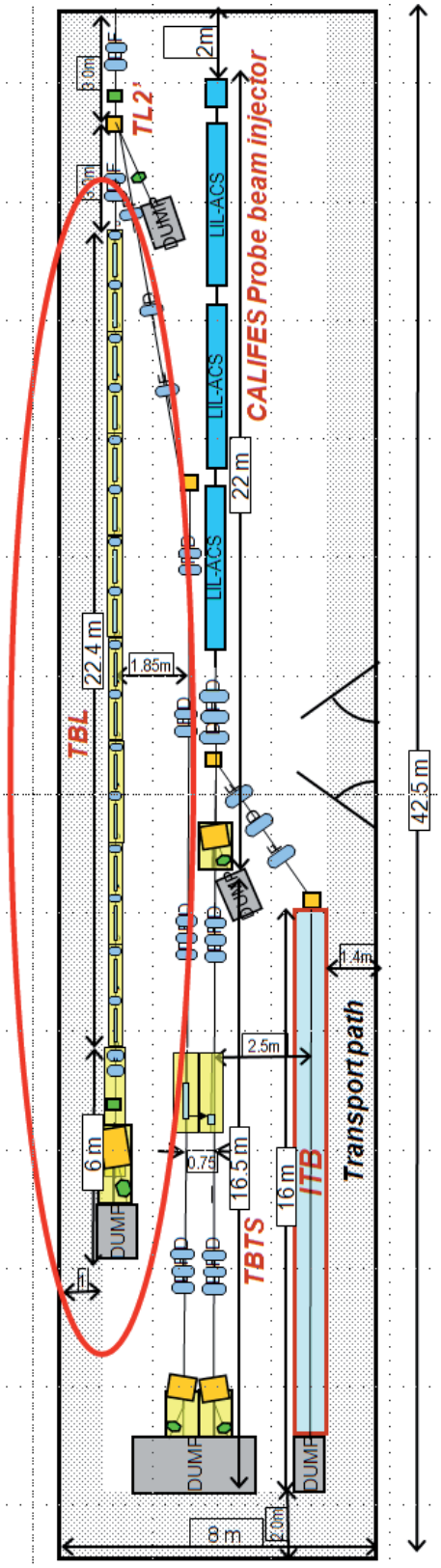

Figure 1.5: Layout of the CLEX building area where the TBL is located (top).

1.2 The CLIC Test Facility 3 and the Test Beam Line in the CLEX area

.

An important milestone will be the proof-of-principle demonstration that major CLIC technologies are feasible. The 3^{rd} generation CLIC test facility (CTF3) [3], currently under construction, should demonstrate the main CLIC-specific issues by 2010.

CTF3 consists of a 150 MeV electron linac, followed by a series of two rings, the delay loop and the combiner ring (figure 1.4). This part of CTF3 is a scaled-down version of the complex required to generate the CLIC drive beam. It will demonstrate the principle of the novel bunch-interleaving technique using RF deflectors to produce the compressed drive-beam pulses. In CTF3 the compressed beam, with an energy of 150 MeV, 32 A of nominal beam current, a microbunch spacing of 83 ps (12 GHz) and a pulse length of 140 ns, is then sent into the CLIC experimental area (CLEX, figure 1.5). This houses the Test Beam Line (TBL) and a two beam test stand where the CLIC acceleration scheme will be tested, including the extraction of RF power from the drive beam and transfer of this RF power to the accelerating structure, which will accelerate a *probe beam* in a full demonstration of the CLIC acceleration principle.

Main differences between the CTF3 beam and the CLIC drive beam are the energy and the current. The CLIC drive beam has a beam current of 100 A and is decelerated from 2.3 GeV to 0.23 GeV giving up 90% of its energy. Whereas the CTF3 drive beam has a beam current of 32 A and is decelerated from 150 MeV to 0.15 Mev giving up also 90% of its energy.

Construction of CTF3 started after the closure of LEP in 2001, taking advantage of equipment from LEP's pre-injector complex. Its installation is on schedule: the linac, delay loop and combiner ring have already been operated with beam, and further commissioning is on going. The new CLEX building is now ready, with most of the equipment installed, and it saw beam on August 2008.

The main aims of the Test Beam Line (TBL) sub-project of CTF3 are (figure 1.5) [4]:

- to study and demonstrate the technical feasibility and the operation of a drive beam decelerator (including beam losses), with the extraction of as much beam energy as possible. Producing the technology of power generation needed for the two-beam acceleration scheme,
- to demonstrate the stability of the decelerated beam and the produced RF power by the PETS, and
- to benchmark the simulation tools in order to validate the corresponding systems in the CLIC nominal scheme.

Therefore, it will be studied the transport of a beam with a very high energy spread, with no significant beam loss and suppression of the wake fields from the PETS. Additional goals for TBL are the test of alignment procedures and the study of the mechanical layout of a CLIC drive beam module with some involvement of industry to build the PETS and RF components, like waveguides. Finally TBL will produce RF power in the GW range which could be used to test several accelerating structures in parallel.

The TBL line will consist of a series of FODO lattice cells and a diagnostic section at the beginning and end of the line to determine all relevant beam parameters. Each cell is comprised of a quadrupole, a BPM and a PETS (see fig. 1.6). Each quadrupole will be equipped with remotely controlled movers for beam based alignment. The FODO lattice was chosen because of its energy acceptance. Due to transient effects during the filling time of the PETS the first 10 ns of the bunch train will have a huge energy spread from the initial energy down to the final energy of the decelerated beam. The lattice is optimized for the decelerated part of the beam, higher energy particles will see less focusing. The betatron phase advance per cell is close to the theoretical value of 90 degrees per cell for a round beam.

The available space in CLEX allows the construction of up to 16 cells with a length of 1.4 m per cell. A schematic of a TBL cell, with the BPS prototype is shown in figure 1.6. The TBL starts after the first bending magnet of the chicane toward the two beam test stand. The diagnostic section in front of the bending magnet will be used for TBL experiments to determine the beam properties at the entrance of TBL, but is formally (schedule and budget) a part of Transfer Line 2 (TL2). Therefore, TBL starts with a matching section consisting out of a quadrupole doublet, a BPM and a pair of correctors to allow for parallel displacement of the beam to excite wake fields in a controlled way. The matching section is followed by 16 identical cells as described above consisting out of a quadrupole, a BPM and a PETS structure. At the end of the beam line a diagnostic section is installed allowing a characterization of all relevant beam parameters. The section consists of a quadrupole doublet and an Optical Transition Radiation (OTR) screen dedicated to transverse beam profile and emittance measurements. A spectrometer with an angle of 10 degrees and a second screen will provide a measurement of the energy and energy spread. It is planned to install a segmented beam dump enabling time resolved energy measurements. The section is completed by a BPM and a Beam Profile Radio-frequency monitor (BPR, button pick-up type). The BPR will provide a signal proportional to bunch length. The total length of the line is about 32 m. Vacuum valves are foreseen after the bending magnet and before the diagnostic section at the end of the line. The 16 cells will be a single vacuum sector.

The PETS and the quadrupole movers are developed by CIEMAT (Madrid), the BPMs by IFIC (Valencia), in strong collaboration with UPC (Barcelona) responsible for BPMs external amplifiers, as the Spanish contribution to CTF3. The BPMs will be a scaled and adapted version to the TBL specifications of an Inductive Pick-Up (IPU) installed and tested in the Drive Beam Linac (DBL) of CTF3. The first phase of the IFIC collaboration for the TBL line in the CTF3 was to develop two IPU prototypes, called Beam Position Small/Spanish monitor (BPS, see figure 1.7), and in this work it will be described the design, construction and the performance characterization tests of the BPS prototypes [5]. The second phase of the IFIC contribution will be the construction and performance characterization of a BPS' series with 15 units including its respective mechanical supports, that will be installed in the complete TBL line. A rough and schematic schedule to build the TBL is shown in the figure 1.8.

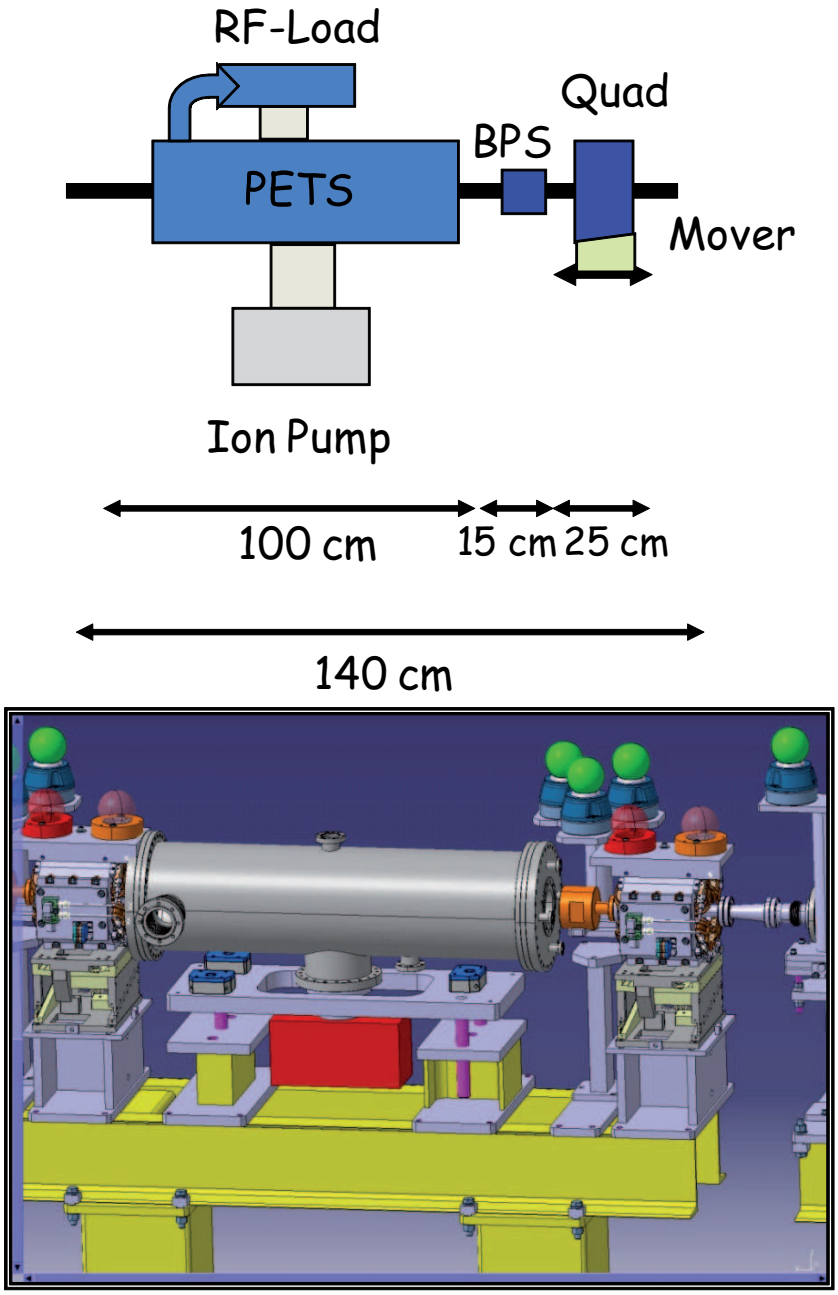

Figure 1.6: Schematic (top) and a 3D view (bottom) of a TBL cell with a PETS tank, the BPS monitor, and a quadrupole.

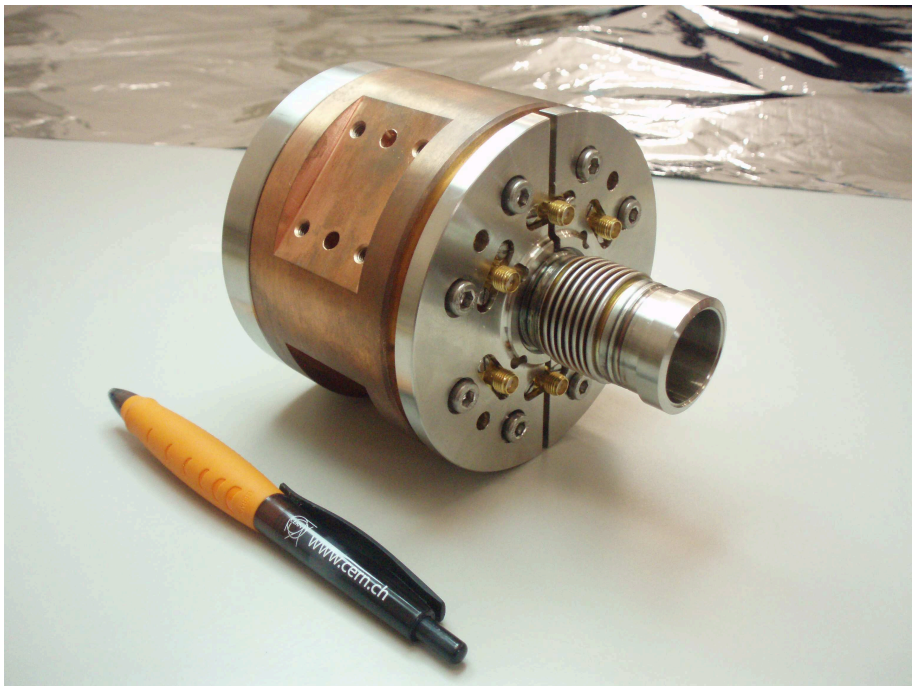

Figure 1.7: View of the BPS first prototype (BPS1).

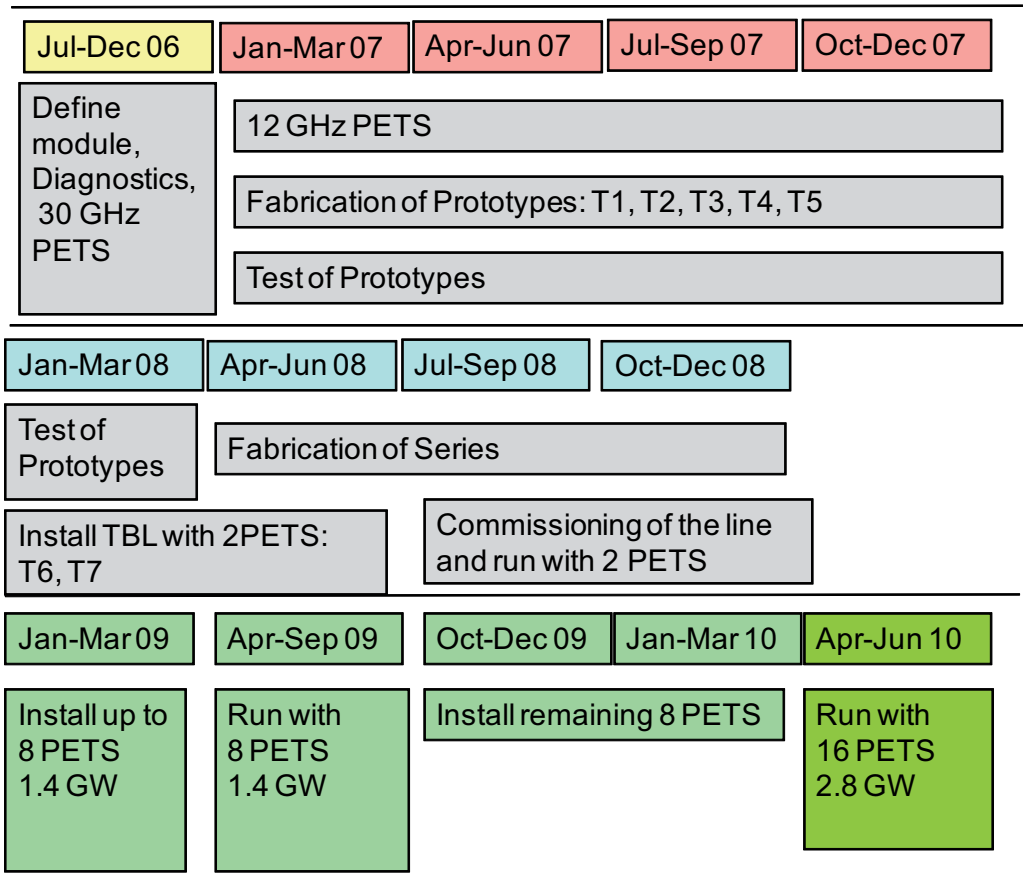

Figure 1.8: Tentative schedule to build the test beam line (TBL) of CTF3.

Chapter 2

Beam Position Monitor. The BPS Monitor Prototype in the TBL

2.1 Beam position monitors in the beam diagnostics field

.

The beam diagnostics is an essential constituent of any accelerator machine. It is the part of the accelerator instrumentation that senses the great variety of beam parameters or properties, so it yields all the necessary information to the accelerators control room that shows the behavior, characteristics and performance of the beam inside the accelerator. It deals with the real beam produced by a real machine including all possible imperfections of a such complex technical installation. Since generally a beam inside the vacuum pipe of an accelerator is very sensitive to any deviation from the accelerator design and it has a very narrow margin of stability, without adequate diagnostics one would "blindly grope around in the dark" for the accelerator settings, and improvements would be hardly achievable.

To achieve a desired performance of the accelerator and thus a good beam specifications, the machine control must be implemented, correcting essentially the parameters of the magnetic elements which drive the beam to the right settings. In the feedback control loop the beam diagnostics will serve as the input of the correction calculation. Depending on the reaction time requirements of the beam property to correct, an automatic feedback control could be implemented or, simply, a control room operator close the loop changing the machine settings for those that do not need fast and periodic control. An example is the reading of the beam position and the correction of the orbit to its nominal value changing properly the magnets parameters.

There is a large variety of beam parameters to be measured. For a good alignment and stability of the beam all relevant parameters should be controllable. Some examples of important beam parameters to be controlled are: the intensity, the transversal and longitudinal profile (size and shape of the beam bunches), the energy and the position. They can be measured by several beam diagnostics devices like: beam transformers, wall-current monitors, pick-ups (PUs) or Faraday cups for measuring the beam intensity; PUs, Secondary Emission Monitors (SEM) grids or wire scanners for transverse profile; and, the same devices as the beam intensity for the longitudinal profile. Figure 2.1 shows an instrumental assembly installed behind the heavy ion linac at GSI during its commissioning [6].

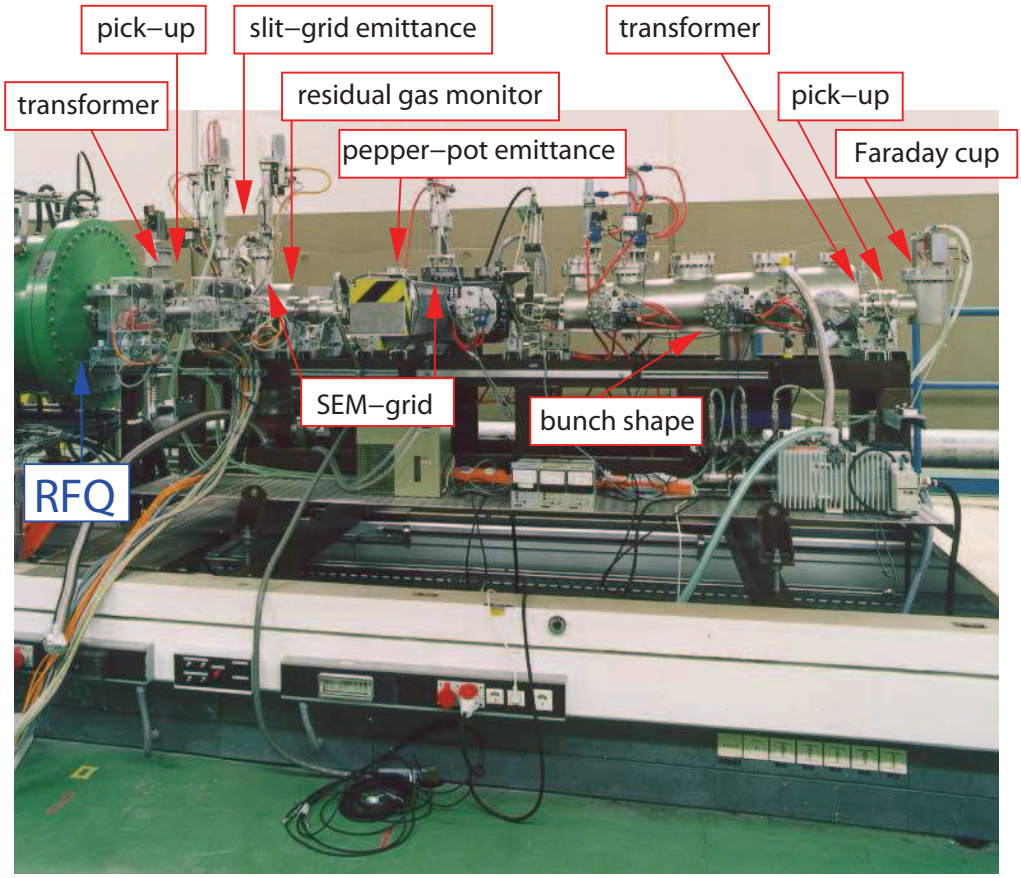

Figure 2.1: View of an accelerator movable test bench with several beam diagnostics instrumentation devices, provided for commissioning of the new high current RFQ (Radio-Frequency Quadrupole) of GSI (green tank on the left). Courtesy of Gesellschaft für Schwerionenforschung (GSI), Darmstadt, Germany.

Usually one kind of diagnostic device can be used to measure several beam properties, like the pick-ups in the previous example. In the same way, for measuring a particular beam property one has to choose the most suitable diagnostic device, always depending on the features of the beam and the type of accelerator. For some beam properties, the type of instrumentation differs for linacs and synchrotrons, due to their different accelerating principles. An important example is, that in a linac or a transfer line, the beam passes only once, while in a synchrotron the behavior of thousands of passages have to be determined. Moreover, electron beams have a quite different behavior as compared to protons or heavy ions. A simple example is the fact, that electrons are relativistic just after the first LINAC modules, while for protons several hundred meters long linacs or even a synchrotron is needed to reach significant relativistic conditions.

Under the denomination of Beam Position Monitors (BPMs) there are all the types of diagnostics devices that can measure, as its primary purpose, the transverse beam position inside the accelerator vacuum pipe. The beam position is one of the beam properties that can be measured for a great diversity of diagnostics devices. The most popular and widely used in the case of bunched beams are the PUs [7], because of their relative simply design and high reliability features, apart from being a non-intercepting sensing method that is

preferred whenever is possible to do not degrade the beam.

All the types of PUs are based on electromagnetic effects. For instance, the capacitive PUs which are of the electrostatic type, and the BPM prototype described in this report which belongs to the inductive or magnetic type, and will be presented in the next section.

2.2 Inductive PU (IPU): The BPS monitor prototype for the TBL

.

Original inductive PUs (IPU) were developed for beam position monitoring at the linacs, injection lines, accumulator ring and transfer lines of the Large Electron Positron Collider (LEP) Pre-Injector (LPI). Also called magnetic PUs, they have sensing electrodes to detect the proximity of the beam. In contrast to the more popular PUs based on electrostatic effects like charge accumulation in the plate-electrodes of the capacitive PUs, the IPUs use a magnetic transformer coupled to the each electrode to sense the variation of the image current flowing through these electrodes as the beam changes its position with respect them, as it will be detailed in the following subsections.

Our IPU prototype, called BPS (Beam Position Small/Spanish monitor), is a scaled and revised version of the IPU developed recently for the Drive Beam Linac (DBL) of the CTF3 [8] [9], since the new BPS design must be adapted to the TBL line dimensions, as well as to the TBL beam characteristics with new performance requirements (discussed in the 2.2.4 subsection)

2.2.1 Basic description and sensing mechanism of an IPU

.

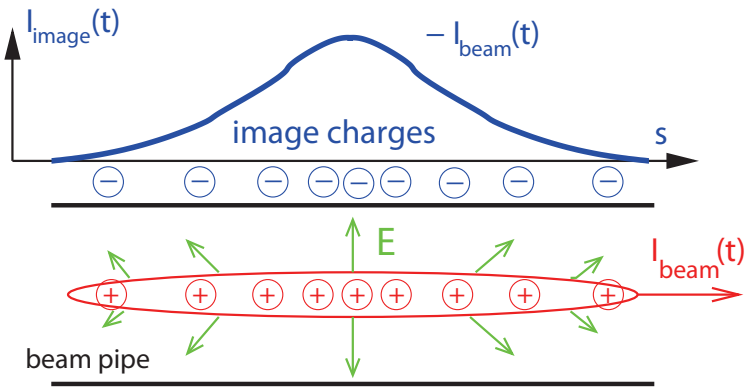

Figure 2.2: Representation of the induced image current by a beam bunch, or wall current, and its intensity profile.

The inductive PU, as many types of PUs, base its sensing mechanism in the wall image current flowing through the conducting vacuum pipe. The beam is a time-varying current since it is composed by bunches of charged particles, and, therefore, it will be accompanied by both a magnetic field and an electric field. In the limit of very high beam energy or relativistic velocities (as it is usually the case of electrons accelerators),

the generated beam fields are pure transverse electric and magnetic, what is known by TEM propagating modes. This TEM fields coming from the beam bunches, as they pass through the conducting vacuum chamber, will induce a wall image current on it. The induced image charges will be of opposite polarity than the beam charges. As a result, each of the beam bunches will produce a transitory image current in the vacuum chamber and its intensity profile will show the longitudinal profile of each beam bunch (see figure 2.2).

In the figure 2.3 it is shown a basic scheme of an IPU longitudinal view which will help to explain the basic sensing mechanism of this BPM. The IPU is designed to let flow the wall image current induced by the beam through its electrodes, and they will be able to sense the wall current azimuthal distribution which will change with the beam position. In this case the pick-up inner wall is divided into four strip electrodes, each of which goes through a toroidal transformer forming the primary winding, as it is depicted in the figure 2.3, in green for the wall image current and in violet for the transformers.

Thus, every wall image current component flowing along each electrode is transformed into a secondary winding, which is connected to a pick-up output through a conditioning circuit on a Printed Circuit Board (PCB). The closer the beam is to the transformer-electrode, the greater is the induced wall current component in the electrode and, in consequence, its output signal amplitude in the secondary winding. This basic sensing mechanism will allow to determine the beam position from the IPU output signals coming through the transformers, and distributed orthogonally around the vacuum pipe aperture, as it is depicted in figure 2.5.

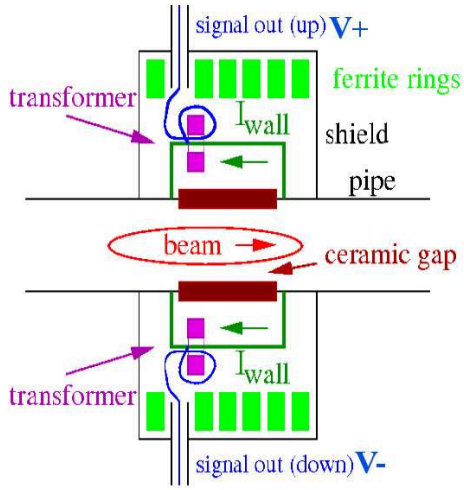

Figure 2.3: IPU longitudinal view scheme, the vertical plane transformer electrodes, V_+ and V_- are depicted.

One must notice that the wall image current intensity flowing through the whole IPU is the same as the beam current intensity but with opposite directions, being $I_{beam} = -I_{wall}$. Therefore, as all the wall current goes through the IPU electrodes, this device will also yield a measure of the beam current intensity by means of the sum of all its output signals, apart from measuring the beam position as its main purpose. Moreover, when the beam is in the centre of the IPU with beam coordinates: $x_V = 0$ for the vertical plane, and, $x_H = 0$ for the horizontal plane; the wall current will be uniformly distributed on the

electrodes and then, the current intensity of each electrode, I_{elec}, will be the same for the four electrodes giving $I_{elec}(x_V = 0, x_H = 0) = I_{beam}/4$.

In a general case for an off-center beam, the current intensity for any electrode, $I_{elec}(x_V, x_H)$, changes as the wall current changes its distribution among the electrodes due to an arbitrary beam position displacement, (x_V, x_H); and it will increase or decrease from the central value, as the beam approaches or move away from the electrode. In the next subsection, it will be described how the beam position is obtained from the IPU output voltage signals which are directly proportional to its respective electrode current, and also will be shown the equations for the linear dependence approximation of the output levels with the beam position.

Finally, just to remark that the electrode current, $I_{elec}(x_V, x_H)$, and, the output signals in a proportional way, present a quite complex non-linear behavior with respect the beam position displacements in the whole IPU aperture, but always it can be approximated to a linear behavior inside a radial region in the vicinity of the center of the IPU aperture; more information is shown in [10]. Therefore, the IPUs are usually designed to keep the beam position range of interest inside the central region of the IPU aperture, where a linear approximation can be performed within acceptable linearity error limits.

2.2.2 IPU output voltage levels and beam position determination

.

It is taken now a closer look to one IPU electrode with a toroidal transformer to better understand its induction sensing mechanism (see figure 2.4). As it was mentioned before, the wall image current will be distributed among the four IPU strip electrodes, and every electrode-end will go through the core of its respective toroidal transformer acting as one-turn primary winding. Consequently, every electrode current component of a time-varying wall image current will induce a current in the secondary circuit, due to the magnetic flux variation produced by this time-varying current in the transformer secondary winding with N_{sec} turns. By the same reason, it must be noted that the transformer is not able to detect dc-current components because these constant current components produces a constant magnitude magnetic field, and so a constant magnetic flux, which can not induce a stationary current in the secondary winding according to the Faraday's law

$$\varepsilon = -\frac{d\Phi_B}{dt}, \tag{2.1}$$

where ε is the electromotive force (in Volts) that would induce a time-varying current in a closed circuit, and Φ_B is the magnetic flux (in Webers). The generated magnetic field from a cylindrical current source (represented in figure 2.4 (left)), as a good approximation of the electrode current, is obtained from the Biot-Savart law

$$\vec{B}(t) = \mu_0 \frac{I_{elec}(t)}{2\pi r} \cdot \vec{e_\varphi}, \tag{2.2}$$

where $\vec{B}(t)$ is the generated time-varying magnetic field, from the electrode current source $I_{elec}(t)$ (assuming a fixed beam position), r is the distance from the source current to the field point, $\vec{e_\varphi}$ is the azimuthal unitary field vector, and μ_0 is the magnetic permeability of the vacuum.

The inductance for a toroidal transformer core of length l in the electrode direction, inner radius r_i and outer radius r_o, having a relative permeability μ_r, and N windings is given by

$$L = \frac{\mu_0 \mu_r}{2\pi} \cdot lN^2 \cdot \ln \frac{r_o}{r_i}. \tag{2.3}$$

then, the toroidal core will guide the magnetic field lines, so only the azimuthal component will be measured.

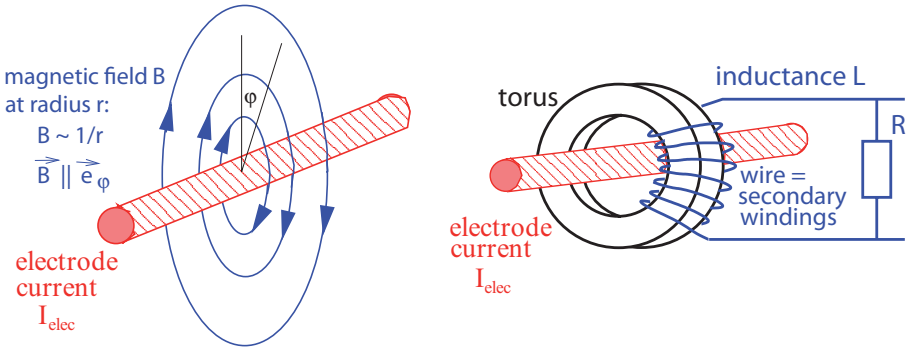

Figure 2.4: Magnetic field generated by the electrode current (left), and the basic scheme of an electrode with its toroidal transformer (right).

Generally, for an ideal current transformer loaded with a low value of ohmic resistance, R, the ratio between the primary current of the electrode, I_{elec}, and secondary current, I_{sec}, is given by

$$I_{sec} = \frac{N_{elec}}{N_{sec}} \cdot I_{elec} \;\Rightarrow\; I_{sec} = \frac{1}{N_{sec}} \cdot I_{elec} \;\; due\ to \;\; N_{elec} = 1, \tag{2.4}$$

with the number of turns on the primary side, N_{elec}, set to one because of the single pass of the electrode through the torus; N_{sec} is the number of turns on the secondary winding which is an important IPU parameter design and, for simplicity, it will be called N further on.

From the circuit scheme of the transformer-electrode (figure 2.4 (right)) a parallel or shunt resistor, R, is introduced leading to the output voltage level proportional to the electrode current for this transformer-electrode

$$V_{sec} = R \cdot I_{sec} = \frac{R}{N} \cdot I_{elec}, \tag{2.5}$$

this relation stands for the frequency components of the electrode current signal in the pass-band of the secondary transformer circuit, above the low cut-off frequency that would introduce the transformer inductance in parallel with the shunt resistor. In the 2.2.3 subsection the ideal frequency response behaviour of an IPU will be presented.

In the figure 2.5 it is depicted the four voltage signal outputs coming from the electrodes secondary winding, V_{sec}, for denoting any of them. And, implicitly in eq. (2.5), their output voltage levels directly depend on the beam proximity to each electrode through the electrode current intensity, I_{elec}, increasing as the induced current intensity of each electrode gets higher with a closer beam.

Thereby, the vertical and horizontal beam position variation will be detected by the two pairs of electrode outputs, $\{V_+, V_-\}$, and $\{H_+, H_-\}$, respectively, and the beam position coordinates will be determined by the difference between these output pairs, being: ΔV, the difference signal for the vertical plane coordinate, and ΔH, the difference signal for the horizontal plane coordinate. Moreover, in order to make the position measurement independent of the beam current, both Δ signals are normalized to the sum of all the electrode output signals, Σ, which is directly proportional to the beam current intensity and, at the same time, independent of beam position. Then, the vertical and horizontal beam position coordinates will be given by

$$\begin{aligned} x_V \propto \frac{\Delta V}{\Sigma} &= \frac{V_+ - V_-}{V_+ + H_+ + V_- + H_-} \ (\textit{Vert. plane}); \\ x_H \propto \frac{\Delta H}{\Sigma} &= \frac{H_+ - H_-}{V_+ + H_+ + V_- + H_-} \ (\textit{Hor. plane}). \end{aligned} \tag{2.6}$$

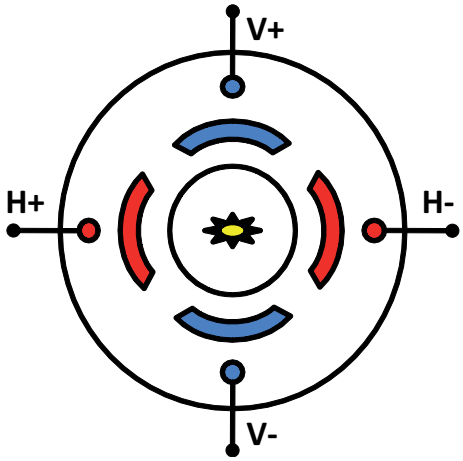

Figure 2.5: IPU schematic transversal view showing the signals outputs with a beam in the center of the vacuum pipe.

This method, commonly used in many pick-ups, for deriving the normalized beam position signal from the raw IPU electrode signals, is called the difference-over-sum (Δ/Σ) processing. And the three ΔV, ΔH and Σ signals will be obtained from an external amplifier connected to the IPU outputs, as it will be shown in the section 2.3 when describing the particular BPS read-out chain.

As it was discussed at the end of previous subsection, the electrode output signals and, also, the Δ signals will show a good linear behavior for the beam position variation within the central region of the IPU aperture. Therefore, a linear fit will be used to characterize the IPU and, thus, obtain the beam position coordinates from the presented signals. The linear relation to give the beam position coordinates from the Δ and Σ voltage signals for the vertical (x_V) and horizontal (x_H) planes are

$$x_V = EOS_V + k_V\left(\frac{\Delta V}{\Sigma}\right) \text{ (}Vert.\ plane\text{)};$$
$$x_H = EOS_H + k_H\left(\frac{\Delta H}{\Sigma}\right) \text{ (}Hor.\ plane\text{)};$$
(2.7)

where $k_{V,H}$ are the characteristic slopes which depend on the IPU sensitivity to the beam position changes in each plane, and $EOS_{V,H}$ are the electric off-sets from the IPU mechanical center for both coordinates. Like the electric off-sets, the IPU sensitivity for each coordinate plane are important characterization parameters and from eqs. (2.7), they are defined as $S_{V,H} \equiv 1/k_{V,H}$. The sensitivity for each coordinate plane, $S_{V,H}$, gives the variation of ΔV or ΔH signals (since Σ is a constant normalization parameter) when the beam changes its position in the vertical or horizontal directions.

Usually in the IPU characterization tests, the position is known and the Δ/Σ parameters for both planes are obtained. Therefore, the sensitivity parameters are obtained from the inverted linear fit equations or characterization equations shown below

$$\left(\frac{\Delta V}{\Sigma}\right) = n_V + S_V\, x_V \text{ (}Vert.\ plane\text{)};$$
$$\left(\frac{\Delta H}{\Sigma}\right) = n_H + S_H\, x_H \text{ (}Hor.\ plane\text{)};$$
(2.8)

where $x_{V,H}$ are the positions, and $n_{V,H}$ are the Δ/Σ parameters deviation when the beam is in the center, which are directly related to the electric off-sets defined in eqs. (2.7). One has to take into account that the sensitivity is defined as a characteristic parameter of the IPU, so the Δ and Σ signals must have the same gain factor to get the true sensitivity of the IPU, or if it is not the case, the measured sensitivity must be divided by the Δ/Σ gain ratio.

The most important parameter to establish the goodness of an IPU performance is the overall precision or accuracy, which can be defined as the ability to determine the position of the beam relative to the particular device being used for measuring the beam position [10]. This is limited by some combination of mechanical alignment errors, mechanical tolerances in the IPU, calibration errors in the electronics, attenuation and reflections in the cables connecting the pickup to the electronics, electromagnetic interference, and circuit noise. All these effects are reflected in the position errors which are deviations from the ideal IPU linear behaviour. From the linear fit eqs. (2.7) can be performed an error analysis to yield the linearity errors of each position which are assumed to follow a gaussian distribution with a standard deviation, σ, and they will represent the uncertainty in measuring the absolute beam position. Then, the overall precision or accuracy of an IPU is obtained as the root mean square (RMS) linearity error, or variance, of all the position errors in the beam positions range of interest for the vertical and the horizontal plane, σ_V and σ_H, respectively.

The resolution is another performance parameter that differs from accuracy in that it

refers to the ability to measure small displacements of the beam, as opposed to its absolute position [10] (see fig. 2.6); so it will represent the minimum displacement or beam position variation the IPU can detect. Typically, the resolution of a system, specifically an IPU, is much better (lower) than the accuracy, being the accuracy as low as the resolution for the best performance case. Furthermore, the IPU position resolution will be lower for larger output voltage levels (of the electrode outputs and Δ signals) since, for a given beam displacement, the difference between those voltage levels will increase allowing a smaller displacement detection. Therefore, as the output voltage levels are directly proportional to the beam current intensity, the resolution must be given for a certain beam current intensity, yielding the best IPU resolution performance at maximum current operation.

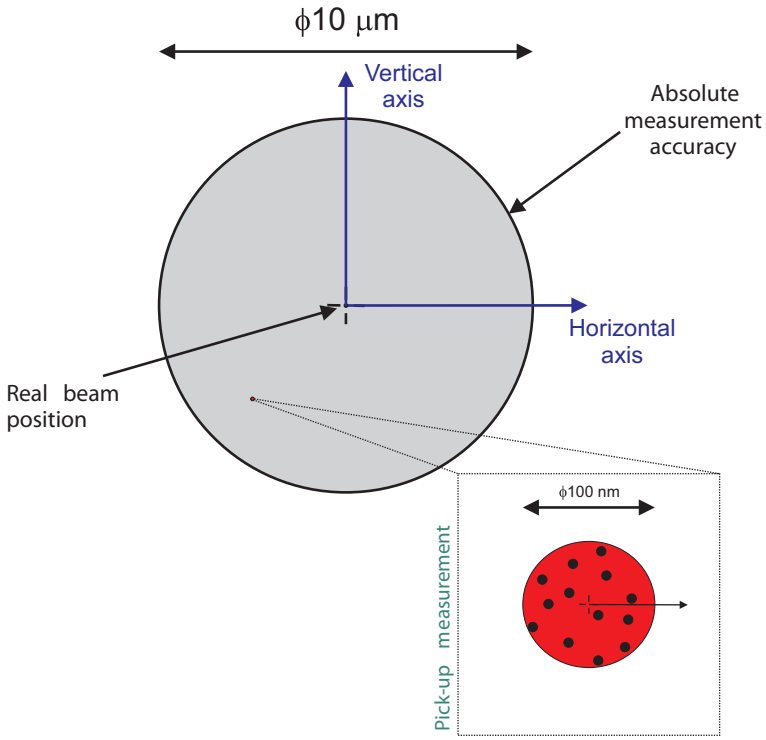

Figure 2.6: Illustration of the difference between the resolution and the overall precision/accuracy parameters of an IPU [9]. For both coordinate planes, the gray circle represents the accuracy (10 μm) and the red one the resolution (0.1 μm) of a particular IPU. Readouts of the same beam position are depicted as black dots.

2.2.3 IPU frequency response and signal transmission

.

The IPU transmission behavior of any arbitrary time-varying input signal, like the beam current signal, can be analyzed in the frequency domain, without loss of generality, by means of the Fourier superposition principle, which states that any signal are a composition of multiple frequency harmonics. So, the beam current harmonic will be of the form, $I_{beam} = I_0(\varphi)e^{i\omega t}$, with angular frequency, ω=2πf, containing the signal frequency, f; and, φ the signal relative phase.

An IPU, like any electromagnetic device, will have a determined output response, in magnitude and phase, for every frequency harmonic of the signal spectrum. Hence, the IPU can be ideally characterized in the frequency domain by its transfer function, defined as the ratio of the output over the input signal, for a given frequency harmonic; and, then, obtaining its typical frequency response pattern by the evaluation of the transfer function magnitude and phase in the frequency band of interest.

Then, the transfer function is obtained from the ratio between the usable output signal voltage, V_{sec}, and the input electrode current, I_{elec}, having dimensions of impedance. Therefore, the transfer impedance, Z_t, for an IPU can be calculated from the equivalent impedance in the transformer secondary equivalent circuit approximation of figure 2.7, being the output voltage signal at a fixed frequency for each electrode,

$$V_{sec}(\omega) = Z_t(\omega) \cdot I_{sec}(\omega) = \frac{Z_t(\omega)}{N} \cdot I_{elec}(\omega), \tag{2.9}$$

and the IPU transfer impedance,

$$Z_t(\omega) = \frac{i\omega L}{1 + i\omega L/R + i\omega L/R \cdot i\omega RC_S}, \tag{2.10}$$

where the transformer secondary winding is modeled as a current source, I_{sec}, in parallel with the inductance, L, of the transformer secondary winding calculated from eq. (2.3). And the capacitor in parallel, C, represents the stray capacitance present between the transformer secondary windings. This transfer impedance is given for a general case assuming an ideal primary electrodes with very low inductances and no coupling between them, so the frequency response is only determined by the transformer secondary circuit.

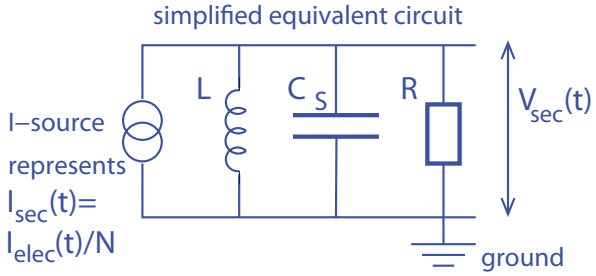

Figure 2.7: Transformer secondary winding equivalent circuit.

From a qualitative analysis of the transfer impedance expression (2.10), it can be obtained the typical frequency response pattern, and its characteristic frequencies, for a general IPU device. Therefore, in the following the transfer impedance asynthotic response is obtained for the frequency ranges of interest:

- **Low frequency range**, assuming $\omega << \frac{R}{L}$:
  In this case, the second and third term in the denominator of eq. (2.10) can be neglected. The resulting transfer impedance is then,

$$Z_t \rightarrow i\omega L. \tag{2.11}$$

  The meaning of this equation is, that the usable output signal at the resistor R decreases proportional to the excitation frequency because the inductance acts as a

short-circuit for the considered low frequencies. In particular, at $\omega = 0$ no signal is recorded. This reflects the well known fact, that a transformer can not handle dc-currents.

- **High frequency range**, assuming $\omega >> \frac{1}{RC_S}$:
  In this case, the third term in the denominator of eq. (2.10), scaling with the frequency square, gets much bigger than the first and second term, so the last can be neglected. The transfer impedance is then,

$$Z_t \rightarrow \frac{1}{i\omega C_S}. \tag{2.12}$$

  Due to the complementary behavior of the inductance and the capacitance, for high frequencies the current is mainly flowing through the capacitor, acting almost like a short-circuit, and therefore the voltage drop at the resistor R will be very low.

- **Pass-band frequency range**, assuming $\frac{R}{L} << \omega << \frac{1}{RC_S}$:
  For this frequency range the second term in the denominator of eq. (2.10) dominates and the first and third term can be neglected. Then, the transfer impedance tend to its maximum magnitude, R, in the middle of the pass-band, and in the whole region is,

$$Z_t \approx R. \tag{2.13}$$

  This is the usable working region, since the voltage drop at the output resistor, R, is significant and proportional to its value. Therefore, in the pass-band frequency region or working region will stand the relation (2.5) of the output voltage level for each IPU electrode, presented previously.

From the previous asynthotic analysis of the transfer impedance, it can be distinguished two characteristic frequencies which are the low cut-off frequency, ω_{low}, and the high cut-off frequency, ω_{high}, corresponding to the lower and the upper boundary of the pass-band, respectively. In a general case, the criterion to determine both cut-off frequencies is at $1/\sqrt{2}$ (in linear scale), or -3 dB, drop from the maximum magnitude of the transfer function, delimiting exactly the bandwidth of the pass-band region. In the case of our transfer impedance, the cut-off frequencies, that agree the last criterion, are defined in terms of the circuit elements as

$$\omega_{low} = \frac{R}{L} \qquad \omega_{high} = \frac{1}{RC_S}, \tag{2.14}$$

and, thus, the bandwidth of the pass-band, or working region, can be very broad, $\omega_{low} << \omega_{high}$, by selecting the appropriate values of the electronic elements.

As the transfer impedance represents a 2^{nd} order passive circuit, there is another characteristic frequency called the resonance frequency, which corresponds exactly to the point of the maximum transfer impedance magnitude, R, and is defined as

$$\omega_{res} \equiv \sqrt{\omega_{low}\,\omega_{high}} = \frac{1}{\sqrt{LC_S}}, \tag{2.15}$$

where the first is a general definition for a RLC $2^n d$ order passive circuit, which states that the resonance frequency is the geometric average of the bandwidth interval (placed in the middle for a logarithmic frequency scale); and, in second place is written in terms of the circuit elements. The resonance frequency can be identified in the third term of the denominator of the transfer impedance expression (2.10), using the cut-off frequencies relations (2.14).

In the figures 2.8 and 2.9, it is represented the ideal IPU frequency response pattern, in magnitude and phase, respectively. These plots are obtained by the evaluation of the modulus and phase of the transfer impedance in a given frequency range. Then, in order to get its magnitude and phase expressions, the transfer impedance can be written, operating from its expression in eq. (2.10), in a more convenient form with separated terms of R_t, as the real or resistive part and, X_t, as the imaginary or reactive part,

$$Z_t(\omega) \equiv R_t(\omega) + iX_t(\omega) = \frac{R}{(1 + F^2(\omega))}\,(1 + iF(\omega))\,, \tag{2.16}$$

where the $F(\omega)$ term contains the frequency dependence of the transfer impedance, and it is written in terms of the cut-off frequencies as

$$F(\omega) \equiv \left(1 - \frac{\omega^2}{\omega_{low}\,\omega_{high}}\right)\frac{\omega_{low}}{\omega}, \tag{2.17}$$

or, likewise, in terms of the circuit elements, just by substituting the cut-off frequency relations (2.14) into the previous expression,

$$F(\omega) \equiv R\left(\frac{1}{L\omega} - C_S\,\omega\right). \tag{2.18}$$

Thereby, taking the modulus of the new transfer impedance form (2.16), the magnitude of transfer impedance (fig. 2.8) can be written as

$$|Z_t(\omega)| = \frac{R}{\sqrt{1 + F^2(\omega)}}, \tag{2.19}$$

which has Ω units, but it is usually represented in dB units just by making $20\log(|Z_t(\omega)|)$. And, the phase of the transfer impedance (fig. 2.9), is simply written as

$$\phi_t(\omega) = \arctan(F(\omega)); \tag{2.20}$$

taking into account that ω=$2\pi f$, for eqs. from (2.16) to (2.20), the same expressions can also be written for the frequency variable, f, making the change, $\omega \rightarrow f$.

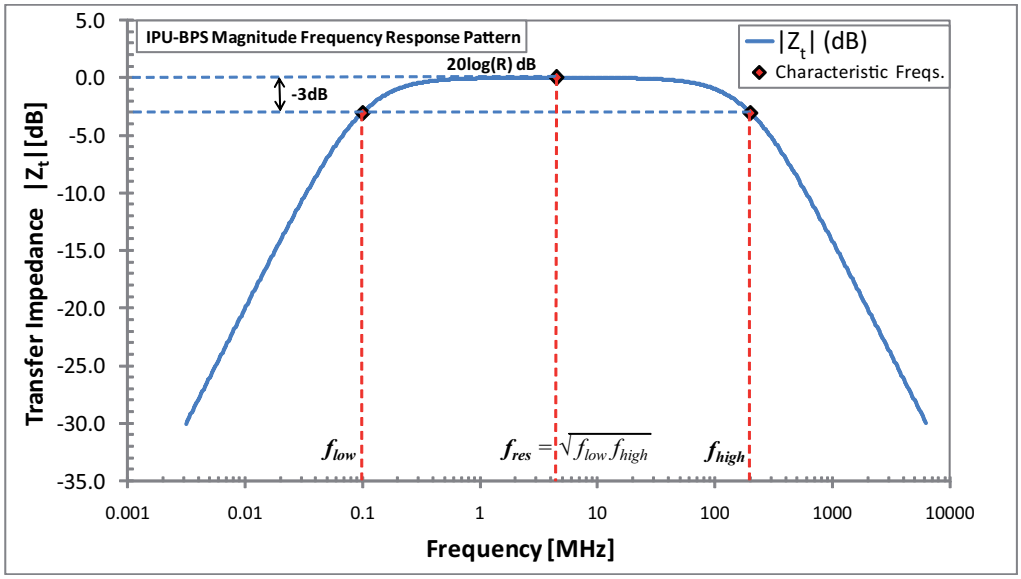

Figure 2.8: IPU typical frequency response pattern of the transfer impedance magnitude. There is also marked with red dots the magnitude of the three characteristic frequencies: the low and high cut-off frequencies, f_{low} and f_{high} respectively, which delimit the IPU bandwidth and are defined at -3 dB drop from the maximum magnitude; and, the resonance frequency, f_{res}, in the middle of the bandwidth as the geometric average of the cut-off frequencies.

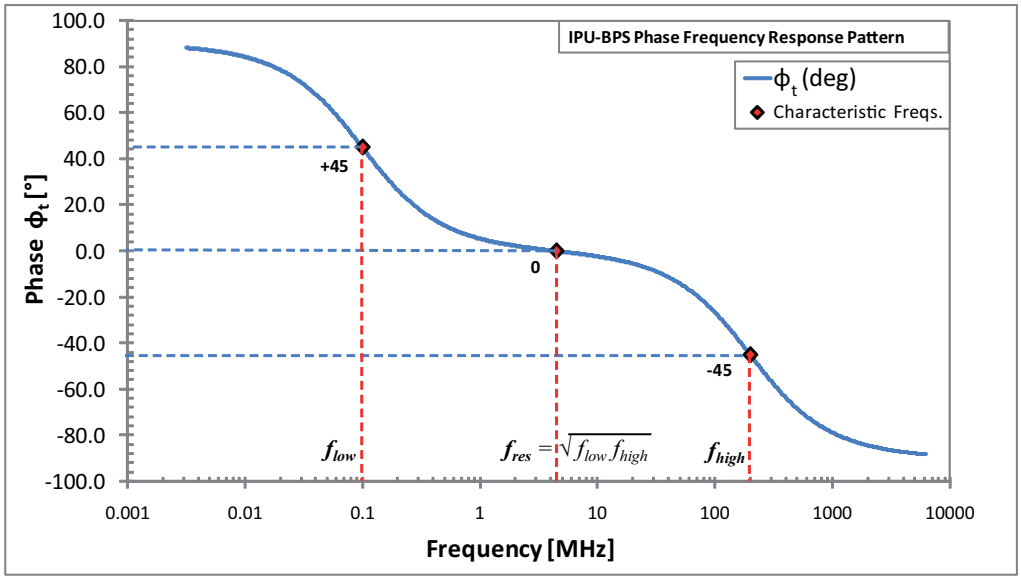

Figure 2.9: IPU typical frequency response pattern of the transfer impedance phase. There is also marked with red dots the middle point in the phase transitions which occur at the low and high cut-off frequencies, and the resonance frequency.

Now, using the eqs. (2.19), (2.17) and (2.20), it can be calculated the values of magnitude (depicted in dB units in fig. 2.8) and phase (depicted in degrees in fig. 2.9) for the characteristic frequencies:

- **Low cut-off frequency**, $\omega = \omega_{low}$:

  if $\omega_{low} << \omega_{high}$, then $F(\omega_{low}) = 1 - (\omega_{low}/\omega_{high}) \approx 1$
  $\Rightarrow |Z_t| = R/\sqrt{2}$, and $\phi_t = \pi/2$;

- **Resonance frequency**, $\omega = \omega_{res} \equiv \sqrt{\omega_{low}\,\omega_{high}}$:

  $F(\omega_{res}) = 0 \Rightarrow |Z_t| = R$, and $\phi_t = 0$;

- **High cut-off frequency**, $\omega = \omega_{high}$:

  if $\omega_{low} << \omega_{high}$, then $F(\omega_{high}) = (\omega_{low}/\omega_{high}) - 1 \approx -1$
  $\Rightarrow |Z_t| = R/\sqrt{2}$, and $\phi_t = -\pi/2$.

Finally, in the frequency response analysis, the secondary equivalent circuit of the IPU electrode, represented by the transfer impedance, could lead to undesirable oscillations for a frequency components close to the resonance frequency, because, as it was mentioned before, this circuit is a 2^{nd} order RLC that could have a resonant behavior. To avoid this, one must be sure that the circuit element values, through the transfer impedance, are far away from giving a resonant frequency response behavior. Therefore, the IPU secondary circuit design must fulfill the following condition to have a non-resonant behavior,

$$\omega_{high} > 2\omega_{low} \quad \Leftrightarrow \quad R^2 < \frac{L}{2C_S}, \tag{2.21}$$

where the second equivalent condition in terms of the circuit values is easily obtained substituting the cut-off frequencies definitions of eqs. (2.14) in the first condition. This particular non-resonance condition can be derived from the more general form for a 2^{nd} order RLC circuit in the Laplace domain,

$$\left\| \frac{\mathrm{Re}(p_0)}{|p_0|} \right\| > \frac{1}{\sqrt{2}}, \tag{2.22}$$

where p_0 can be either of the two complex poles of the transfer impedance expression (2.10) evaluated in the Laplace domain, $Z_t(p)$ (just by making the variable change, $i\omega \rightarrow p$), which is a more general complex plane using the Laplace variable, $p \in \mathbb{C}$; $|p_0|$ and $\mathrm{Re}(p_0)$ are the modulus and the real part of the poles, respectively.

A more relaxed condition would be, if the poles of the transfer impedance were purely real, then, $|p_0| = \mathrm{Re}(p_0)$, and there would be no resonance since the general condition (2.22) is fulfilled. As a result, turning to the particular non-resonance condition (2.21), the resonant behavior would be avoided by selecting a low value for the output resistor, R, and a high secondary transformer inductance, L, resulting in an over-damping of possible oscillations may appear, and, also, increasing the bandwidth of the IPU; as it is the case represented in figs. 2.8 and 2.9.

On the other hand, turning to time domain, the limited bandwidth of the IPU frequency response will affect to the transmitted beam signal shape, as it is shown in the figure 2.10 for a beam pulse, and a beam bunch. Since the beam position measure will be

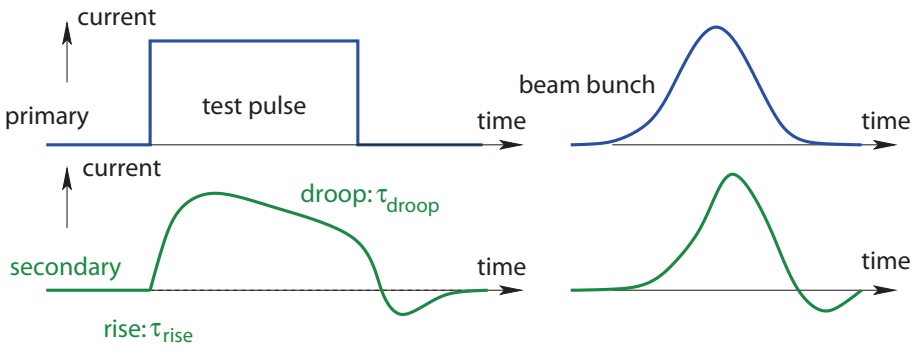

Figure 2.10: Time response to a beam signal shape.

proportional to the amplitude of the transmitted signal, the IPU must let pass the signal shape without too much deformation. As a consequence two time parameters are defined from the characteristic cut-off frequencies

$$\tau_{droop} = \frac{1}{\omega_{low}} \qquad \tau_{rise} = \frac{1}{\omega_{high}}; \tag{2.23}$$

and, substituting the cut-off frequencies depending on the secondary components,

$$\tau_{droop} = \frac{L}{R} \qquad \tau_{rise} = RC_S\,. \tag{2.24}$$

These characteristic time parameters, τ_{rise} and τ_{droop}, corresponds, respectively, to the exponential setup and decay characteristic times of a pass-band type circuit response, when it is excited with a step-wise function like a beam pulse signal.

Usually for a square-pulsed beam, the droop time parameter, τ_{droop}, is the most important since the beam position measure will be sampled from the transmitted pulse signal, and it must have a pulse top as flat as possible, in a pre-determined time interval, to do not have different signal measurement in the same pulse. As a rule of thumb, the droop time constant might be hundred times larger than the beam pulse duration, t_{pulse}, to have a good flat-top pulse response, so $\tau_{droop} \sim 10^2 t_{pulse}$.

2.2.4 TBL line and BPS specifications

.

The IPU can be used for all type of accelerators, from linacs to synchrotrons accelerating electrons, protons or ions. But they are mainly used for bunched beams with short pulses, typically between 1 ns and 10 μs, because of the pulse droop for larger pulses described before. Moreover, the beam velocities must be close to the speed of light to have a TEM beam field getting, thus, a good sensitivity of the wall image current distribution with the transversal beam position. The bunching structure of a beam could also be observed in time, if the bunches were larger than 1 ns, what would corresponds to achieve an IPU bandwidth up to 500 MHz or τ_{rise} of 0.3 ns, so they are considered broadband BPMs.

Centering in the TBL line of CTF3 and its beam position monitoring needs, the IPU type was considered the most suitable. There were several reasons for choosing and developing an IPU, based on magnetic sensing, rather than a more conventional electrostatic

one like the capacitive pick-up. The IPU is less perturbed by the high losses experienced in linacs; the total length can be short for horizontal, vertical and sum measurements; it generates high output voltages for typical beam currents in the range of amperes; and calibration wire inputs allow testing with a simulated beam current.

The table 2.1 [11] summarizes the main TBL beam characteristics, including also the BPM parameters specification that our IPU prototype, called BPS, must fulfill. The electrons beam arriving to the TBL are injected at 150 MeV close to relativistic velocities, and the beam pulse duration or, what is the same, the bunch train duration is short, t_{pulse} between 20 ns and 140 ns, so the IPU type fits good with the requirements of proper IPU working conditions, as it was mentioned before. The TBL beam time structure is shown in the figure 2.11 to see more clearly the time parameters specification of the TBL beam.

TBL Beam Parameters	
Beam current range	1–32 A
Bunch train duration, t_{pulse}	20–140 ns
Injection beam energy	150 MeV
Microbunch spacing	83 ps(12 GHz)
Microbunch duration	4–20 ps
Microbunch charge	0.6–2.7 nC
Repetition frequency	0.83–50 Hz
Radiation level	≤1000 Gray/year
Emittance	150 μm
BPM Parameters	
Analog bandwidth	10 kHz–100 MHz
Beam position range	±5 mm (H/V)
Beam aperture diameter	24 mm
Overall mechanical length	126 mm
Number of BPM's in TBL	16
Resolution at maximum current	≤5 μm
Overall precision (accuracy), $\sigma_{V,H}$	≤50 μm

Table 2.1: TBL Beam Parameters and BPM characteristics.

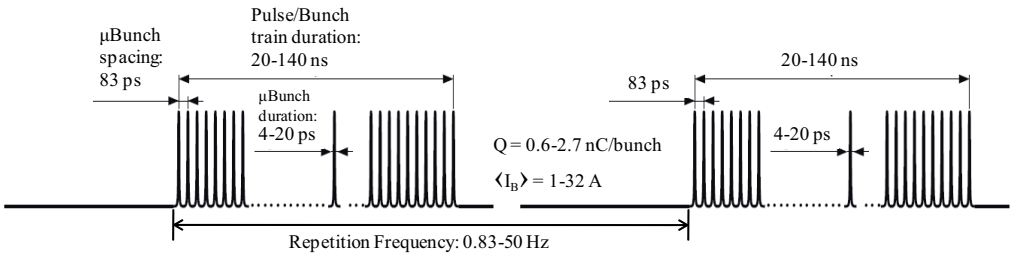

Figure 2.11: TBL beam time structure.

The BPS prototype is intended to determine the beam position at beam pulse time scale, so it will not be able to observe at the microbunch level (duration between 4–20 ps), because it would need a bandwidth up to 250 GHz, what is obviously too high.

Concerning the analog bandwidth requirements, the high cut-off frequency is set to

f_{high} = 100 MHz, so using eqs. (2.23), the rise time constant is τ_{rise} = 1.6 ns, which will have a fast pulse edge response when the beam pulse edge arrives, compared with the pulse duration, t_{pulse} = 140 ns, since $\tau_{rise} \sim 10^{-2} t_{pulse}$ = 1.4 ns. On the other hand, the τ_{droop} related with the low cut-off frequency, f_{low}, must be much larger than the pulse duration, in order to get a desired flat response of the transmitted pulse, as it was discussed in the previous subsection. Thus, for f_{low} = 10 kHz corresponding to a droop time constant, τ_{droop} = 16 μs, will give a slow pulse decay having a good flat response for t_{pulse} = 140 ns, being $\tau_{droop} \sim 10^{2} t_{pulse}$ = 14 μs.

2.3 BPS beam position read-out stages description

.

The BPS output signals are $\{V_+, V_-\}$, for the vertical plane, and $\{H_+, H_-\}$, for the horizontal one, but the beam position coordinates are obtained by means of the difference signals, ΔV and ΔH for each plane, and normalize them to the sum signal, Σ, [12] as it was mentioned in the subsection 2.2.2.

This processing work will be done by an external amplifier connected to the four BPS signal outputs. It will have three channels corresponding to the ΔV, ΔH and Σ signals, and because a great signal variation range is expected in the Δ channels, from mili-volts to tens of volts, they will have two amplification modes, high gain and low gain, and even one attenuation mode. For the Σ signal as it is constant for a given beam current will be only attenuated due to its high level, or enough level in the case of 1 A, the minimum beam current operation [13].

These amplification or attenuation modes will be selected from the control room with a dedicated configuration signals, and it must be done to adapt the amplifier output signal levels to the fixed range of input levels of the digitalization stage. In the figure 2.12 it is depicted the complete read-out chain to get the signals of the beam position coordinates displayed in the control room monitors.

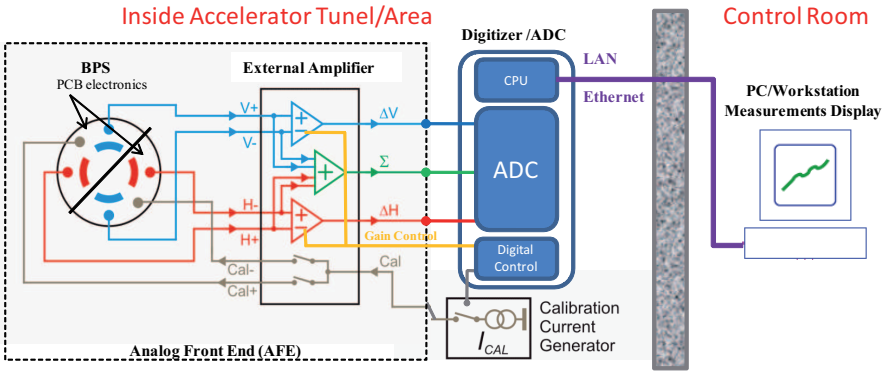

Figure 2.12: Beam position complete read-out stages.

The tandem BPS and the external amplifier forms what is called the Analog Front End (AFE) of the beam position read-out chain. The parameters of both devices in the AFE are strongly coupled and therefore some BPS design choices will be related to the

amplifier design, and vice versa. As a consequence, some BPS characteristics will be often discussed jointly with the amplifier ones, later on the next chapters.

In the next chapter where the BPS electronic design will be presented, the BPS circuit for the two calibration current signals, shown in the figure 2.12, are described in detail. But now, just to say that the BPS calibration inputs are used for exciting the transformer secondary winding like the wall current flowing through each electrode would do it, and thus calibrate the BPS output signals without a real beam from the control room.

An important issue when designing electronics for being close to the accelerator is that the electronics must resist the ionizing radiation coming from the beam losses, or alternatively, the electronic components must have a radiation hardness (rad-hard) specification or a maximum radiation dose that guarantee their good performance during a time period. For the TBL line case the maximum radiation level present in the accelerator area is 1 KGray per year, specified in the table 2.1. Therefore all the components of the devices inside the TBL area must have at least this rad-hard specification. For the BPS electronics mounted on a PCB there is no problem because it has only passive components and their performance are much less affected by radiation than the integrated circuits (ICs) and the SMD thick film resistors used are rad-hard enough. Nevertheless, for the amplifier and the digitizer components must be guaranteed that they are rad-hard to the level specified for the TBL.

Chapter 3

Mechanical and Electronic Design of the BPS Prototype

3.1 Mechanical Design and Construction

.

The IPU mechanical design is considered one of the most complex among the pick-up family. As it was introduced in the section 1.2, the first phase of our collaboration in the TBL line of the CTF3 project, consisted in the design and construction of two IPU prototypes, called BPS1 and BPS2. One of them should be installed in the TBL line and fully operative at the end of 2008. The other one would remain as a spare unit, but also ready to install in case of necessity.

The BPS mechanical design was adapted to the TBL line required dimensions. The BPS parts are depicted in the figure 3.1, and each part, referenced with a letter, is described in the next paragraphs.

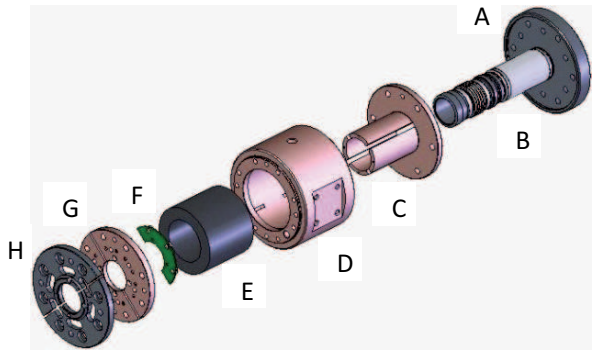

Figure 3.1: View of the BPS prototype parts.

The BPS has a length of 126 mm with a external diameter of 100 mm and an inner diameter of 24 mm for the vacuum chamber. The vacuum assembly (A), consists of a ceramic tube (B) brazed to two Kovar collars at both ends, with one collar TIG welded directly to the downstream flange, and the other one electron welded to a bellow and a rotative flange. In order to minimize the BPS longitudinal impedance and let flow the high frequency components above the bandwidth of interest of the wall image current,

the inside of the ceramic tube is titanium coated using the sputtering technique [9]. The four strip electrodes (C) cover most of the circumference in order to make the BPS as transparent to the beam as possible. In order to decrease the low frequency cut-off , the electrodes are surrounded by a ferrite cylinder (E) inserted in the body (D). The plates (G) accommodate the two PCB halves (F) on which the four transformers are mounted (only one half is shown). A screw passes through each transformer, as its primary winding, and connecting each strip electrode to the plate (G). To achieve good low frequency responses primary circuits parasitic resistances had to be kept below a mΩ, thus the body (D), the electrodes (C) and the plates (G) are made of copper. The plates as well as the beryllium-copper screws are gold plated. The four strip electrodes and the their supporting plates are machined in one piece to minimize contact resistances between small surfaces and to achieve good mechanical precision. There are also four uniformly distributed alignment pins, passing through the plates (G) and inserted in the cooper body (D), which will ensure a correct alignment of the assembled parts, and thus avoiding large linearity errors in the beam position measures.

In the figure 3.2 is shown in more detail the location of the PCB and the golden screws, which extend the strip electrodes in order to pass through the transformers center and behave as the primary winding. Also the wall image current flowing through the strip electrodes is depicted.

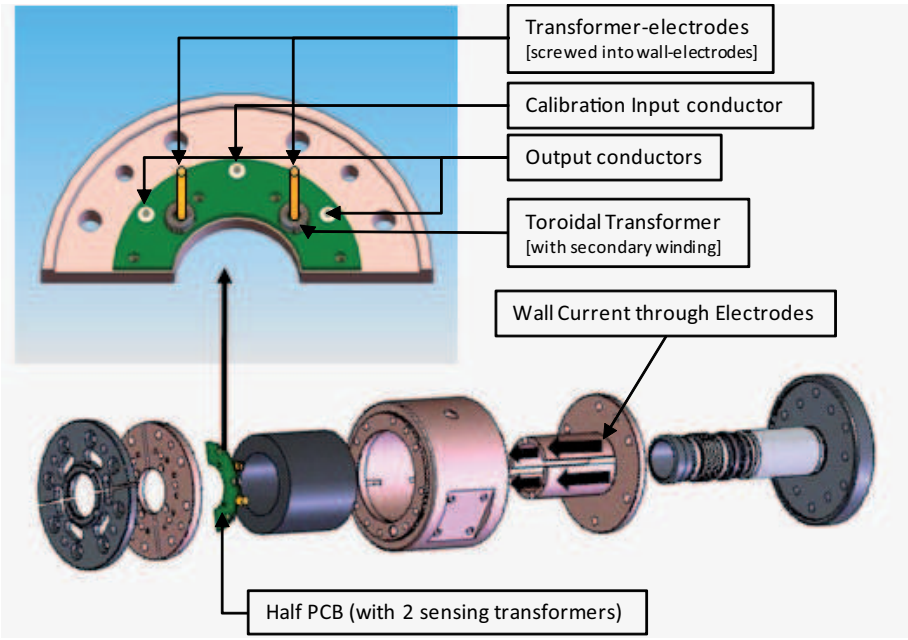

Figure 3.2: Detailed view of a half PCB with two transformers and the golden screws as the primary winding electrode (up). The location of the PCB inside the BPS and the direction of the wall current through the strip electrodes are shown (down).

The BPS real parts and the final assembly can be identified in the figure 3.3. The most critical part of the BPS construction was the vacuum tube assembly (fig. 3.3, down left corner). As the inner part of the BPS and a continuation of the TBL line vacuum pipe where the beam will flow, all the pieces must be perfectly welded to ensure the high vacuum level specified for the CTF3, which is in the order of 10^{-10} mbar.l/s [11]. The

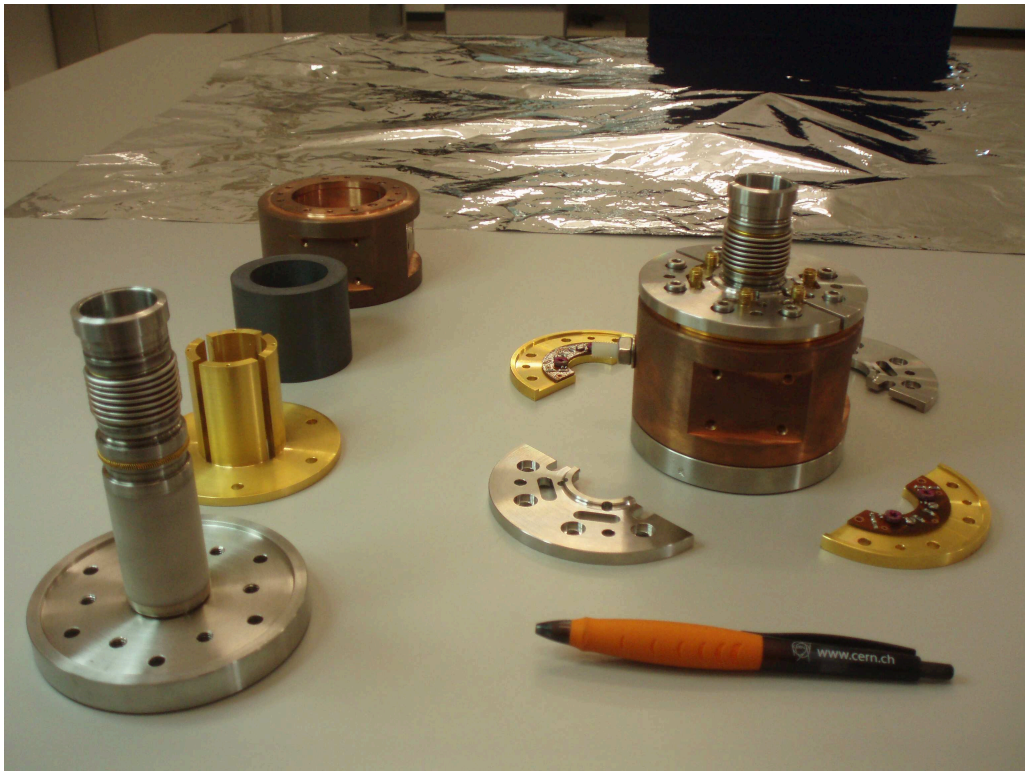

Figure 3.3: The two constructed BPS prototypes, the BPS1 assembled (right) and the different parts of the BPS2 distributed around.

vacuum tests where performed at CERN giving a leak level under specifications for both BPS prototypes. The inner parts of the BPS prototypes, with the vacuum pipe welded to the downstream flange (see fig. 3.3, down-left), was manufactured and assembled by *G&P Vacuum Projects*; and, in *Talleres Lemar* was made the outer BPS parts like the cooper body, the strip electrodes, and the plates.

3.2 Electronic Design

.

As it was introduced in the previous chapter, the four output voltage signals (V_+, H_+, V_-, H_-) will drive an external amplifier to yield three signals for determining the beam position: sum signal ($\Sigma = V_+ + H_+ + V_- + H_-$), proportional to the beam current; and two difference signals ($\Delta V = V_+ - V_-$ and $\Delta H = H_+ - H_-$) for horizontal and vertical plane. There is also two input calibration signals, Cal+ and Cal−, to check the correct function of the sensing PCB halves. In the figure 3.4, it is shown a picture of the BPS prototype where the four signal output ports and the two calibration input ports have their respective names depicted. The connectors used for all the BPS ports are of SMA type. Also in this picture the designed PCBs screwed on the golden plates are shown outside the BPS but keeping the orientation they have when assembled inside the BPS.

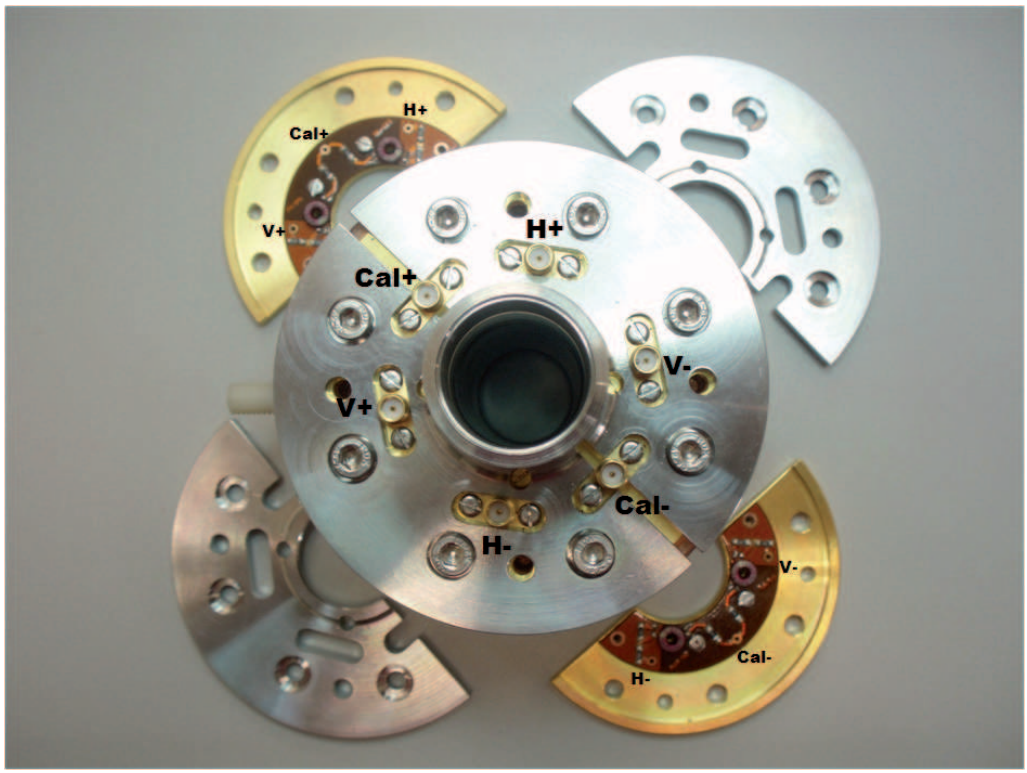

Figure 3.4: Top view of the BPS prototype to show the SMA output ports and calibration input ports, labeled with their names; and the PCBs outside with the toroidal transformers.

3.2.1 Schematic and PCBs layout design

.

The figure 3.5 shows the schematic circuit design for the two PCB halves of the BPS prototype. It can be seen that both halves are completely equivalent. We can identify the calibration primary circuit with one winding turn at the left side of the toroidal transformers coming from the calibration inputs, Cal+ and Cal−; and the transformer secondary circuits, with N turns, connected to the BPS outputs at the right side through a resistors divider. The BPS electrodes are not represented since they cross the PCB and the toroidal transformers, as it is depicted in the figure 3.2, but, of course, each electrode acts also as a primary circuit for the wall image current when sensing the beam position.

The calibration circuits have 50 Ω input resistance (two branches of 100 Ω in parallel) at each input port to match the connected cable. They are used to excite the BPS with pulsed calibration signals of known amplitude which will be equivalent to the electrode wall current signals but of 0.1% amplitude level. Then, from the control room (see figure 2.12) the operators will be able to calibrate and check the performance of the BPS and the amplifier Δ and Σ channels without beam. This is important, since the external amplifier are only one meter away from the beam line and it is exposed to some radiation. The calibration signals, Cal+ and Cal−, will excite each half PCB corresponding, respectively, to a pair of outputs, the positive, V_+ and H_+, and the negative ones, V_- and H_-. Hence, when exciting only one calibration input, say Cal+, this will be equivalent to a have the beam in a equidistant position from the V_+ and H_+ electrodes. Similarly, when exciting

both calibration inputs with identical signals, it will be equivalent to have a centered beam. This situation is also useful to check the common mode rejection ratio (CMRR) of the amplifier Δ channels, because they should get a zero output and only noise will be present.

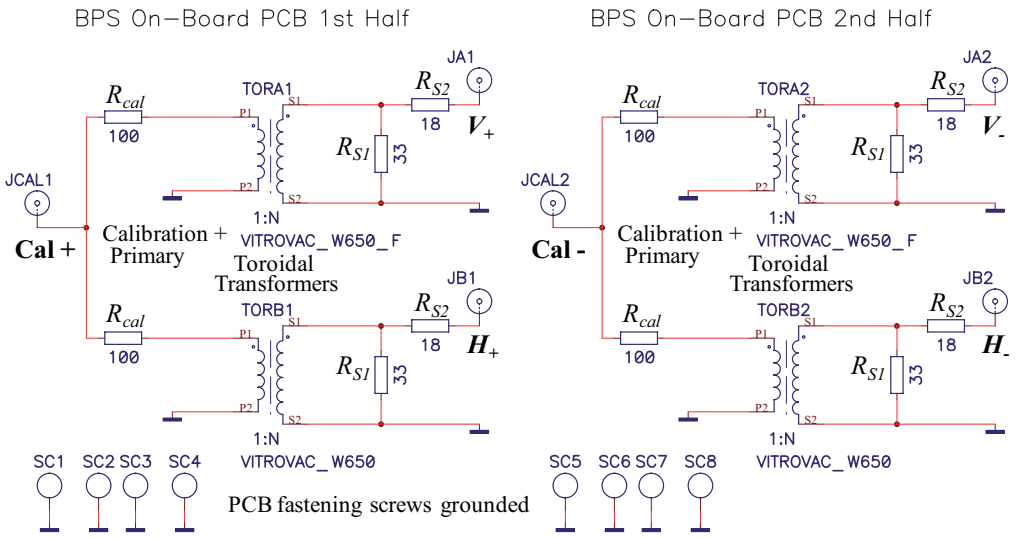

Figure 3.5: PCB schematic circuit design.

In order to get the basic BPS output voltage relations in the pass-band, we consider each transformer electrode current, I_{elec}, exciting its respective secondary circuits, shown in the schematics (fig. 3.5), and inducing a secondary current, $I_{sec} = I_{elec}/N$, using the ideal transformer relation with N turns from (2.4). And, from the secondary circuit of the schematics with the resistors, R_{S1} and R_{S2}, but taking into account the resistor loads, $R_{Load} = 50\ \Omega$, when the outputs are connected, we can obtain the output voltage relation for the BPS, equivalent to the general relation (2.5) for the IPU,

$$V_{sec} = \left(\frac{R_{S1}R_{Load}}{R_{S1} + R_{S2} + R_{Load}}\right) I_{sec} = \left(\frac{R_{S1}R_{Load}}{(R_{S1} + R_{S2} + R_{Load})N}\right) I_{elec}, \tag{3.1}$$

where V_{sec} stands for V_+, H_+, V_- or H_- BPS outputs, the transformer current relation (2.4) has been used. In order to match the output resistance to the load, avoiding possible signal reflections at high frequencies, and, at the same time, be able to select freely the output voltage level with the resistor value, R_{S1}; the resistor divider of the secondary circuit must fulfill the condition, $R_{S1} + R_{S2} = R_{Load} = 50\ \Omega$. In this case, the general output relation (3.1) is simplified, and can be written as

$$V_{sec} = \left(\frac{R_{S1}}{2N}\right) I_{elec}. \tag{3.2}$$

Therefore, the output signals will depend on the varying electrode current, as the beam changes its position, and from the more general output relation (3.1) we can also get the sum of the output signals, Σ, as

$$\Sigma = \left(\frac{R_{S1}R_{Load}}{(R_{S1} + R_{S2} + R_{Load})N}\right) I_B, \tag{3.3}$$

where I_B is the total beam image current. So, the sum signal will keep constant in magnitude for a given beam image current in the pass-band frequency response of the BPS. Like for the particular output relation (3.2), the sum signal, Σ, is simplified by matching the output resistor divider to the load, and, then, it is written as

$$\Sigma = \left(\frac{R_{S1}}{2N}\right) I_B. \tag{3.4}$$

Clearly, the proportional factor is the same for the electrode outputs and the sum signal, hence for $N = 30$ turns and $R_{S1} = 33\ \Omega$ as the selected design values, we get the equivalent impedance value, or the output voltage sensitivity to the electrode current variation, as a characteristic parameter of the BPS1, $\Sigma/I_B = 0.55\ \Omega$.

And, also, using eqs. (3.1) and (3.3), the electrode output voltage would be,

$$V_{sec} = \left(\frac{\Sigma}{I_B}\right) I_{elec} = 0.55\Omega\ I_{elec}. \tag{3.5}$$

Once this parameter is fixed, and for a given nominal beam current, say $I_B = 30$ A, we can get some output voltage levels which will help in the external amplifier gain selections in order to adjust these signal levels to the ADC input. These output levels are:

- $\Sigma = 16.5$ V for the sum signal;
- $V_{sec} = \Sigma/4 = 4.125$ V for the four BPS outputs with a centered beam;
- $\|\Delta V\|_{max} = \|\Delta H\|_{max} = \Sigma/2 = 8.25$ V, the estimated maximum output level of the difference signals for each plane, which can be obtained taking differences in the relation (3.5), and as

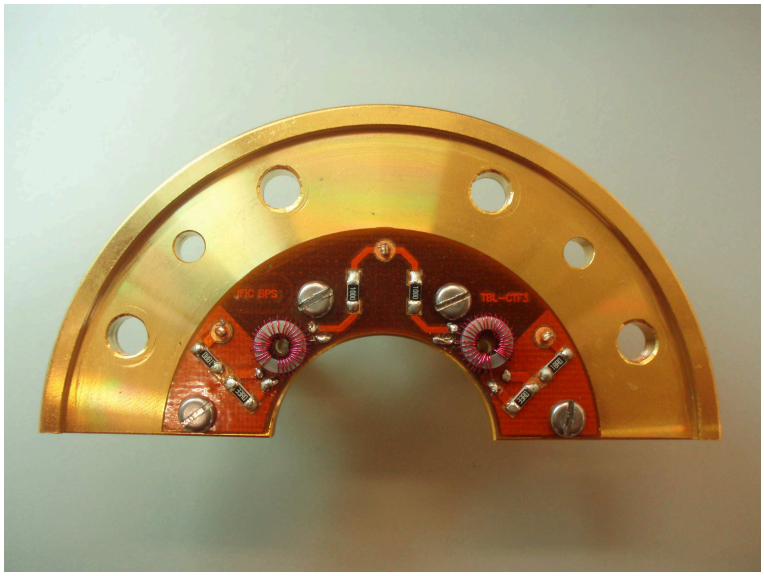

Figure 3.6: View of a mounted PCB prototype with the transformers having one calibration turn and 30 turns in the secondary winding.

In the figure 3.6 it is shown a real PCB prototype with the components mounted, which implements the BPS inductive sensing circuit schematic described before (figure 3.5).

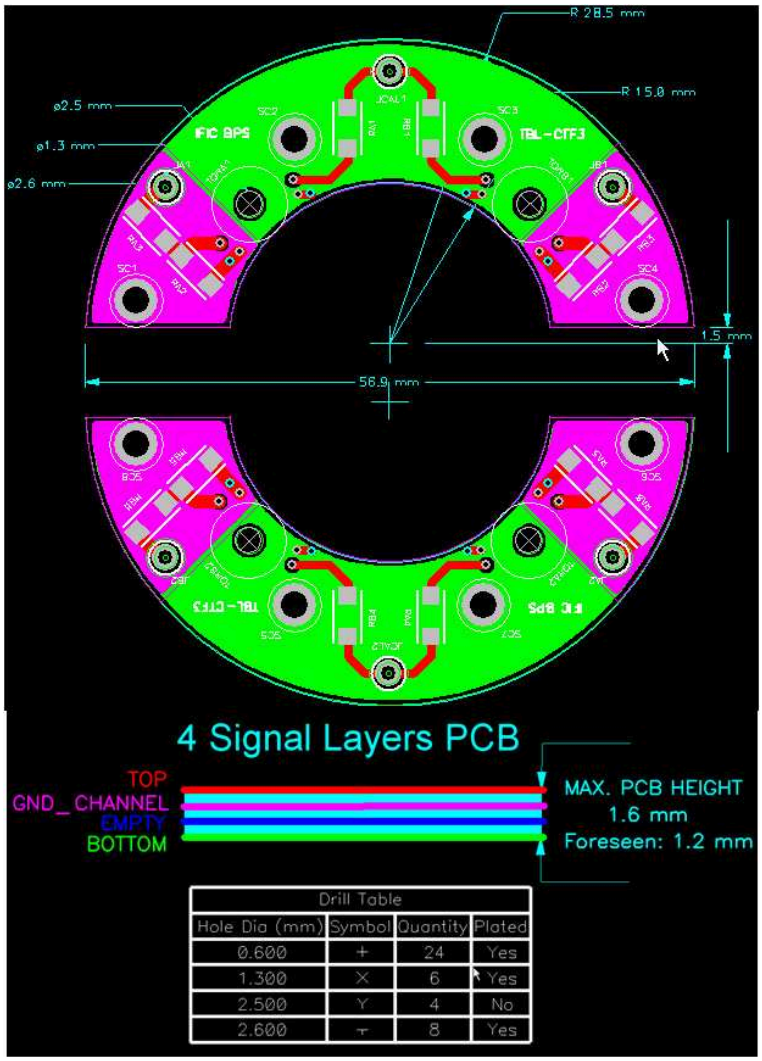

Figure 3.7: BPS PCBs layout with the dimensions, the layers structure and the drill table depicted.

Also, the layout design of the two half PCBs of the BPS is shown in the figure 3.7. The PCB tracks were chosen to have at least 30 mils (approx. 0.8 mm) to reduce as possible the track resistance for currents in the order of 1 A. They have the components layer or top layer (in red), the bottom layer as a ground plane (in green), and an intermediate ground plane (in violet) closer to the top layer. This layer is intended to help in keeping the secondary current return paths concentrated below each transformer secondary circuit, and then reduce the ground coupling in the other secondary circuits when, as the worst case, the current is totally balanced to one electrode.

Notice the room leaved in the PCB layout to place the toroidal transformers (figure 3.7), with circular footprint and holes for the screw electrodes that will act as the primary winding for sensing the beam position. The transformer core, made of a magnetic material called Vitrovac, was chosen to have high relative permeability, μ_r, and then getting high inductance with few turns. In principle, this is important since the low cut-off frequency decrease with a higher inductance according to (2.14). From the relation for a

toroidal shaped transformer (2.3) and knowing the Vitrovac core specifications [14], the inductance per square turn can be determined, $L/N^2 = 35.35\ \mu$H. Therefore, having selected $N = 30$ turns in the transformers secondary winding, the secondary inductance is, $L_{sec} = 31.8$ mH.

3.2.2 BPS electric model and frequency response characterization parameters

.

The particular BPS frequency response analysis will be based on the electric model [8] of the figure 3.8, and it is better to start from the BPS secondary circuits of each transformer electrode, which exhibit a well-established behavior having a pass-band pattern with a bandwidth delimited by the low and high cut-off frequencies, as it was presented in the 2.2.3 subsection for a general IPU.

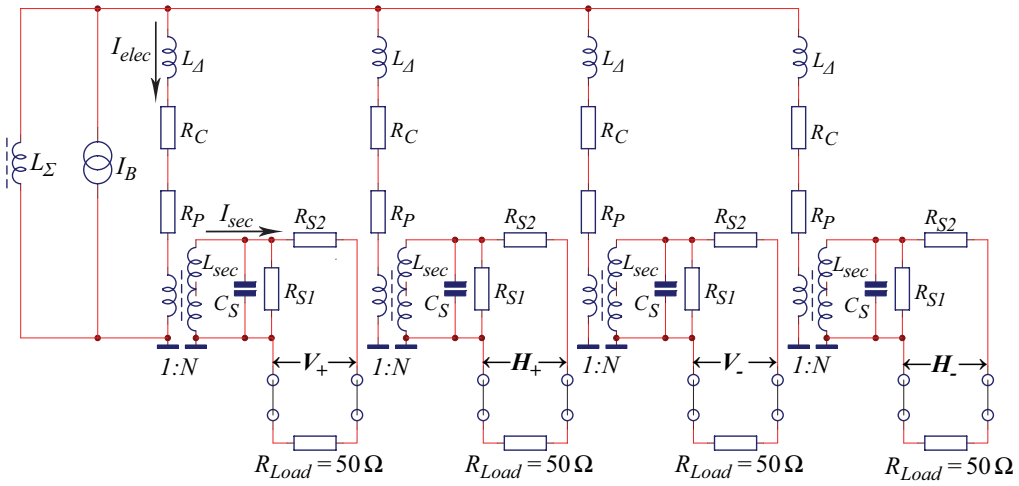

Figure 3.8: Electric model of the BPS which determines its frequency response behavior.

As a first description of the electric model (fig. 3.8), the four strip electrodes with their respective secondary circuits are represented. The current source is equivalent to the beam image current, I_B, and L_Σ is the inductance of the loops made up from the electrodes and the cooper body walls enclosing the outer ferrite cylinder (figure 3.1(E)). The strip electrodes are modeled by each of the branches departing from the current source with the following circuit elements: R_C representing the parasitic resistance of the connections in the BPS assembly, R_P will take account for secondary circuit resistance seen from the primary of the toroidal transformer, and L_Δ for reflecting, in certain cases, an important inductive coupling among the strip electrodes at low frequencies that will be described later.

Then, from the present electric model it can be obtained the transfer impedance for each of the secondary circuits of the BPS,

$$Z_{tsec}(\omega) = \left(\frac{R_{Load}}{R_{S2} + R_{Load}}\right) \frac{i\omega L_{sec}}{1 + i\omega L_{sec}/R_e + i\omega L_{sec}/R_e \cdot i\omega R_e C_S}, \tag{3.6}$$

where L_{sec} is the inductance of the secondary winding with N turns, C_S is the stray capacitance mainly present between the windings of the transformer secondary, and R_e stands for the equivalent resistance of the secondary circuit including the load resistor and in parallel with the stray capacitance, which is

$$R_e = R_{S1} \parallel (R_{S2} + R_{Load}). \tag{3.7}$$

The transfer impedance of the BPS secondary circuits (eq. (3.6)) is essentially equivalent to the transfer impedance for a general IPU (eq. (2.10)), presented in the previous chapter, since they only differ in the resistive factor multiplying the same transfer impedance form, but with the BPS particular circuit components, L_{sec}, R_e and C_S. Furthermore, the output voltage relation (2.9) will remain unchanged, but the actual transfer impedance, Z_{tsec}, is used instead of the former transfer impedance for the IPU.

Therefore, the frequency response pattern of the BPS secondary circuits will be the same as the obtained for the general IPU, and the low and high cut-off frequencies relations will be equivalent to those for the IPU in eqs. (2.14), but now expressed in terms of the BPS secondary circuit elements,

$$f_{low} = \frac{R_e}{2\pi L_{sec}} \qquad f_{high} = \frac{1}{2\pi R_e C_S}, \tag{3.8}$$

where the well-known relation between the frequency parameters, $\omega = 2\pi f$, has been used.

In principle, these cut-off frequencies will delimit the bandwidth of the pass-band region for the BPS, and the transfer impedance will have an approximately constant value in this frequency range. Then, in the pass-band region, the BPS transfer impedance expression (3.6) can be approximated as,

$$Z_{tsec} \approx \left(\frac{R_{Load}R_e}{R_{S2} + R_{Load}}\right) = \left(\frac{R_{Load}R_{S1}}{R_{S1} + R_{S2} + R_{Load}}\right), \tag{3.9}$$

where the equivalent resistance relation (3.7) has been used to get the last expression only in terms of the secondary circuit elements. Moreover, the BPS output voltage relation (3.2) for the pass-band region, presented in the 3.2.1 subsection, can be easily recovered by applying the secondary circuit matching condition, $R_{S1} + R_{S2} = R_{Load} = 50\ \Omega$, to the last expression of the approximated transfer impedance in eq. (3.9), and, then, substituting it into the output voltage relation (2.9).

Again, as it was discussed in subsection 2.2.3, the design values of the secondary circuit in the PCB must be chosen to be far away from a resonant behavior. Hence, the non-resonance condition of eqs. (2.21) must be fulfilled, but now it will be expressed in terms of the BPS secondary circuit elements, using the cut-off frequencies in eqs. (3.8),

$$f_{high} > 2 f_{low} \quad \Leftrightarrow \quad {R_e}^2 < \frac{L_{sec}}{2C_S}, \tag{3.10}$$

hence, although the stray capacitance, C_S, were not known a priori, the design values for the secondary circuit elements were chosen to have a broad bandwidth, with a relatively high secondary inductance, L_{sec}, and low equivalent resistance, R_e, favouring, then, the fulfillment of the non-resonance condition. In specific component values we have: $L_{sec} = 31.8$ mH as it was calculated in the previous subsection, and $R_e = 22.2\ \Omega$

from eq. (3.7) with $R_{S1} = 33\ \Omega$, $R_{S2} = 18\ \Omega$ and $R_{Load} = 50\ \Omega$; yielding from the non-resonance condition (eq. (3.10)) that the stray capacitance should have a maximum value given by, $C_S < 32.2\ \mu$F, what is far above the typical values for these loss capacitances. The last was confirmed when the BPS high cut-off frequency was determined to be above the 100 MHz, as it is presented in the next chapter with of BPS test results, and, as a result, the non-resonance condition is fulfilled by far, since the stray capacitance will be, $C_S < 72$ pF, from the high cut-off frequency relation (3.8) for $f_{high} > 100$ MHz, having a much lower stray capacitance than the maximum value specified before to get a resonant response.

Concerning the BPS behavior at low frequencies, the first tests performed in the BPS suggested to us that the low cut-off frequency was not fixed by the secondary winding inductance, L_{sec}, calculated before. When designing the PCB, this secondary inductance was made large enough to get, according to (3.8), a small low cut-off frequency for each electrode output, and, as a result, have a minimum droop deformation of the transmitted pulse signal. But, indeed, the existing inductances in the electrodes, acting as the primary circuits, were limiting the bandwidth at low frequencies since the involved inductances, L_Σ and L_Δ, are much lower than the secondary inductances, L_{sec}, and they will set higher low cut-off frequencies.

For that reason, in order to justify the behavior of the BPS frequency response at low frequencies, it is needed a deeper analysis performed from the primary circuit side of the four BPS transformer electrodes shown in the electric model. Therefore, the true low cut-off frequency cannot be determined from the first relation in eqs. (3.8), which comes directly from the transfer impedance expression (3.6) applied to each of the BPS secondary circuits treated independently. Nevertheless, the high cut-off frequency relation in eqs. (3.8) will hold for limiting the upper region of the bandwidth, since the BPS behavior at high frequencies is dominated by the stray capacitance present between the transformer secondary windings, and, hence, it is perfectly defined by the secondary circuits transfer impedance.

Now, turning to the primary circuit side of the transformer electrodes, the effect of the secondary circuits in the frequency response is considered by transforming the secondary equivalent impedance, Z_e, seen from the terminals of the transformer winding, into the primary electrodes side as a series impedance, Z_P. Thus, the transformation relation is given by

$$Z_P(f) = \frac{Z_e(f)}{N^2}, \tag{3.11}$$

which represents the secondary impedance seen from the transformer terminals at the primary side. This relation can be derived considering that the toroidal transformer, as an ideal transformer, transmits all the power from the primary to the secondary side, so, $P_{prim} = P_{sec}$, and, jointly, using the ideal transformer relation (2.4) to get the transformation factor between the impedances, $(1/N)^2$, which is the squared ratio of the primary over the secondary number of turns.

The secondary equivalent impedance, Z_e, is the impedance seen from the terminals of the transformer secondary winding and not the transfer impedance, Z_{tsec}, between the secondary current and the output; but, Z_{tsec} only differ from Z_e in the multiplicative factor depending on the resistor values, R_{S2} and R_{Load}, in eq. (3.6). Thus, the secondary equiva-

lent impedance can be written in the more appropriate form of resistive and reactive parts as

$$Z_e(f) = \frac{R_e}{1 + F^2(f)}\,(1 + iF(f)), \quad with \;\; F(f) \equiv \left(1 - \frac{f^2}{f_{low}\, f_{high}}\right)\frac{f_{low}}{f}, \tag{3.12}$$

which is completely analog to the transfer impedance of the general IPU of eq. (2.16), and, as before, the $F(f)$ term (eq. (2.17)) contains all the frequency dependence of the secondary equivalent impedance with the cut-off frequencies of eqs. (3.8).

Thereby, substituting the last expression in eq. (3.11), the resistive and the reactive parts of the secondary transformed impedance seen from the primary side will be

$$Z_P(f) \equiv R_P(f) + iX_P(f) = \frac{R_e}{(1 + F^2(f))N^2} + i\left(\frac{R_e F(f)}{(1 + F^2(f))N^2}\right), \tag{3.13}$$

but the resistive part, R_P, will be the only term of the primary impedance that will contribute significantly to the frequency response at low frequencies, because, as it was discussed before, the inductances involved in the primary side, L_Σ and L_Δ, being much lower than the secondary inductance, L_{sec}, they will limit the lower region of the BPS bandwidth, instead of the low cut-off frequency of the secondary circuit, f_{low}, fixed by L_{sec}. Then, at the low frequencies where the electrodes will attenuate the BPS response, the secondary equivalent impedance will be still in the pass-band region of the secondary circuit, where the frequency term in eq. (3.13), $F(f)$, is very close to zero, and, hence, the reactance of the transformed secondary impedance, X_P, will be negligible.

As a consequence, in the electric model (see fig. 3.8), it is only considered the resistive term of the primary impedance in eq. (3.13), and it is also cancelled its frequency dependence factor, $F(f) \approx 0$, in the pass-band region of the secondary circuit, yielding

$$R_P = \frac{R_e}{N^2} = \frac{R_{S1} \parallel (R_{S2} + R_{Load})}{N^2}, \tag{3.14}$$

for a secondary winding with N turns, and being: R_{S1} and R_{S2}, the secondary circuit resistors, and R_{Load} the external amplifier input resistance when connected to the BPS outputs. For the design values of these secondary circuit elements (presented in subsection 3.1.1), the primary resistor will be, $R_P \approx 25$ mΩ.

It is not easy to analyze the true frequency response behavior of the BPS at low frequencies, and the influence of the different inductances represented in the model by L_Σ and L_Δ. One has to take into account the image current distribution through the electrode primaries depending on the beam position. There are two different cases, when the current is balanced through the four strip electrodes corresponding to a centered beam position; and the unbalanced case, when the current is greater in one electrode due to a closer beam position to it.

Concerning the first case, all the electrodes behave in the same way since the image current is equally distributed among them (balanced-current case), and the electric model will be the same as the one depicted in the figure 3.8, but without the L_Δ inductances that will take effect in the second case. Thus, L_Σ will fix the low cut-off frequencies of each electrode output (V_+, H_+, V_-, H_-), and also of the sum signal (Σ), which does not depend

on the beam position, as it was established in subsection 2.2.2, and its frequency response pattern will remain unchanged with the beam position variation.

Hence, like for ω_{low} in eqs. (2.14), L_Σ in parallel with the series resistance, $R_P + R_C$, yields

$$f_{L_\Sigma} = \frac{1}{2\pi L_\Sigma}(R_P + R_C)\,. \tag{3.15}$$

By the other side, when the beam is displaced in one plane toward one electrode, say V_+, in the vertical plane, the image current through it increases as it is expected, decreasing in the opposite electrode V_- (unbalanced-current case). Consequently, the difference signal, $\Delta V = V_+ - V_-$, can be measured between the vertical plane outputs. Due to this situation of image current imbalance between the two vertical electrodes, the inductances L_Δ must be considered, but not for the horizontal plane electrodes because they are at the same distance from the beam position, and their currents are fully balanced. Likewise, the inverse situation will occurs for the horizontal plane and the ΔH signal. In this way, the L_Δ inductances are used, in each coordinate plane, to model the coupling between opposite electrodes when there is a current imbalance. Therefore, they will fix now the low cut-off frequencies for both difference signals, ΔV and ΔH, since L_Δ will be much lower than the common parallel inductance, L_Σ, getting

$$f_{L_\Delta} = \frac{1}{2\pi L_\Delta}(R_P + R_C)\,. \tag{3.16}$$

This coupling can be better understood considering that the electrodes, when changing the beam position, only are able to detect the high frequency components of image current pulse, varying their amplitudes in consequence. But for the low frequency components, above the electrode cut-off frequency (f_{L_Σ}), their amplitudes keep constant. In another words, the low frequencies of the image current pulse will be always equally distributed through the electrodes, being not sensible to beam position variation, because the image current will be redistributed among the electrodes through their common interconnection points. In consequence, when making the difference of the output signals for each pair of electrodes or coordinate planes, ΔV or ΔH, the lower frequency components of the electrode voltage outputs remain constant in magnitude, and their difference will vanish in this low frequency range, appearing only a difference in magnitude at the higher frequency components, what will yield a higher low cut-off frequencies for the Δ signals. Of course, this behaviour was inferred from the frequency response tests performed to the BPS, and the plot of the figure 3.9 illustrates the discussed coupling effect between the strip electrodes for both coordinate planes.

Finally, turning to time domain, as we discussed in the section 2.2.3, the transmitted pulse will suffer from a exponential droop deformation from the flat-top response due to the defined low cut-off frequencies for the Σ and Δ signals, and also it will have a rise or setup time constant caused by the high cut-off frequency (common to all signals). Then, summarizing for the characteristic cut-off frequencies obtained before, and using the relations in eqs. (2.23), we define

$$\tau_{droop_\Sigma} = \frac{1}{\omega_{L_\Sigma}}, \tag{3.17}$$

as the characteristic droop time from the low cut-off frequency, $\omega_{L_\Sigma} = 2\pi f_{L_\Sigma}$, for the

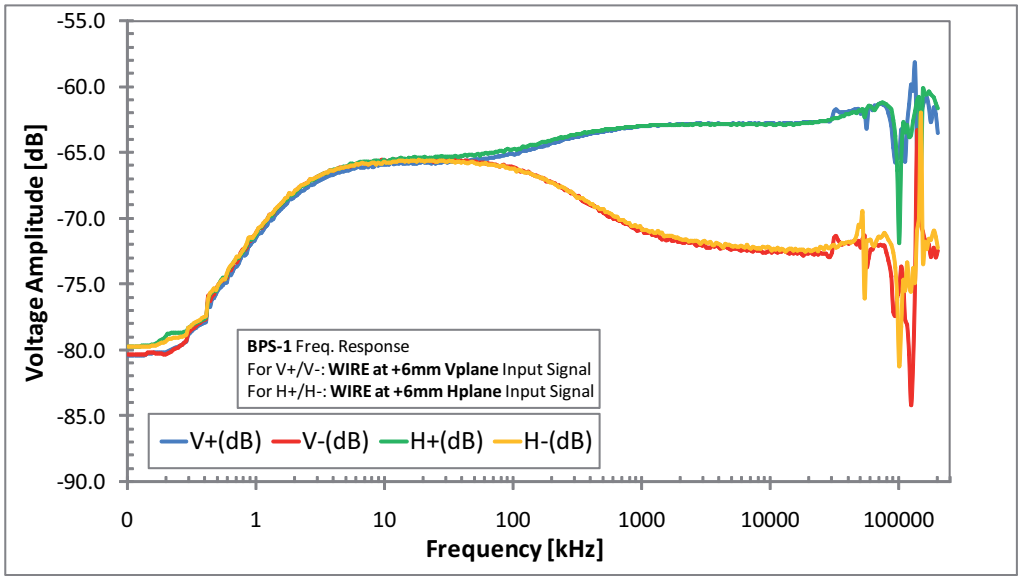

Figure 3.9: BPS1 frequency response for the electrode outputs and two different simulated beam positions (or current wire positions): at +6 mm in the vertical plane, V_+ and V_- are measured; and, at +6 mm in the horizontal plane, H_+ and H_-, are measured. Above the electrode low cut-off frequency, $f_{L_\Sigma} \approx 2$ kHz, the lower frequency components keep constant in magnitude, increasing the low cut-off frequency for the Δ signals, f_{L_Δ}.

Σ signal, and also for the output electrodes with a centered beam;

$$\tau_{droop_\Delta} = \frac{1}{\omega_{L_\Delta}}, \tag{3.18}$$

as the characteristic droop time from the low cut-off frequency, $\omega_{L_\Delta} = 2\pi f_{L_\Delta}$, for the Δ signals, and also for the output electrodes when the beam is out of the center; and, finally,

$$\tau_{rise} = \frac{1}{\omega_{high}}, \tag{3.19}$$

as the characteristic rise time from the high cut-off frequency, $\omega_{high} = 2\pi f_{high}$, for the output electrodes, the Δ and Σ signals.

All the defined low and high cut-off frequencies, and its associated characteristic time constants, can be measured for a beam (or current wire) input excitation, and also for the calibration input excitation, as it will be shown in the next section 4.3 of the BPS1 prototype test results. In both cases, the output signals are generated through the transformer secondary circuits but induced from different primary circuits: the electrodes for beam (or current wire) excitation; and, the calibration turn for the calibration inputs excitation (see fig. 3.5).

Chapter 4

BPS Prototype Characterization Test Results

4.1 The BPS wire test description

.

The tests to characterize the BPS1 prototype performance parameters was realized using a special testbench setup, so called the wire test method. Essentially, this testbench allows moving the BPS with respect to a current wire that simulates the beam passing through the BPS under test. The main aim of the wire test method is to obtain measurements of the sensitivity, linearity and frequency response (bandwidth) of the BPS1 prototype. These tests were carried out during several short stays at CERN, in the AB/BI-PI[1] laboratories [15], where the wire testbench is placed. This setup has been previously used for testing and calibrating the BPMs for the DBL of the CTF3.

As can be seen in figure 4.1, the wire testbench consists in a stage where are installed the BPS1 prototype with its adaptation support. The stage holding this setup is attached to a 3-axis manual positioning structure which has a digital display encoder to read the stage displacement with a ± 5 μm resolution. On the other hand, the top of the wire is soldered to a SMA connector screwed it down to a static roof, which will be the input of the excitation signal. Because the wire has to simulate the beam, it cross the BPS longitudinally and a weight is hanging at the bottom end of the wire to keep it aligned with the BPS longitudinal axis just by gravity (depicted in the figure 4.1 with a dotted line and a blue triangle). This weight is inside a tank floating on mercury in order to make contact with the tank walls and, then, close the circuit of the wire. Because of this, the wire current will have its return path mainly through the BPS body, but, it is worth to remark that the current sensed in the BPS electrodes is not this return current, it actually is the transient image current induced in the BPS conducting walls by the TEM modes of the wire current. Also to mention that in the tank there is oil to allow a soft motion of the weight floating on the mercury when making a platform displacement. Therefore, the current wire will stand still, while moving the platform jointly with the BPS. This procedure of moving the BPS instead of the wire is preferred because, making wire displacements to a certain position would cause oscillations in the wire after reach this position, so it would be necessary to wait each time until they stop completely.

[1]CERN AB/BI-PI: Position and Intensity (PI) Section of the Beam Instrumentation Group (BI) from the Accelerators and Beams Department (AB) of CERN.

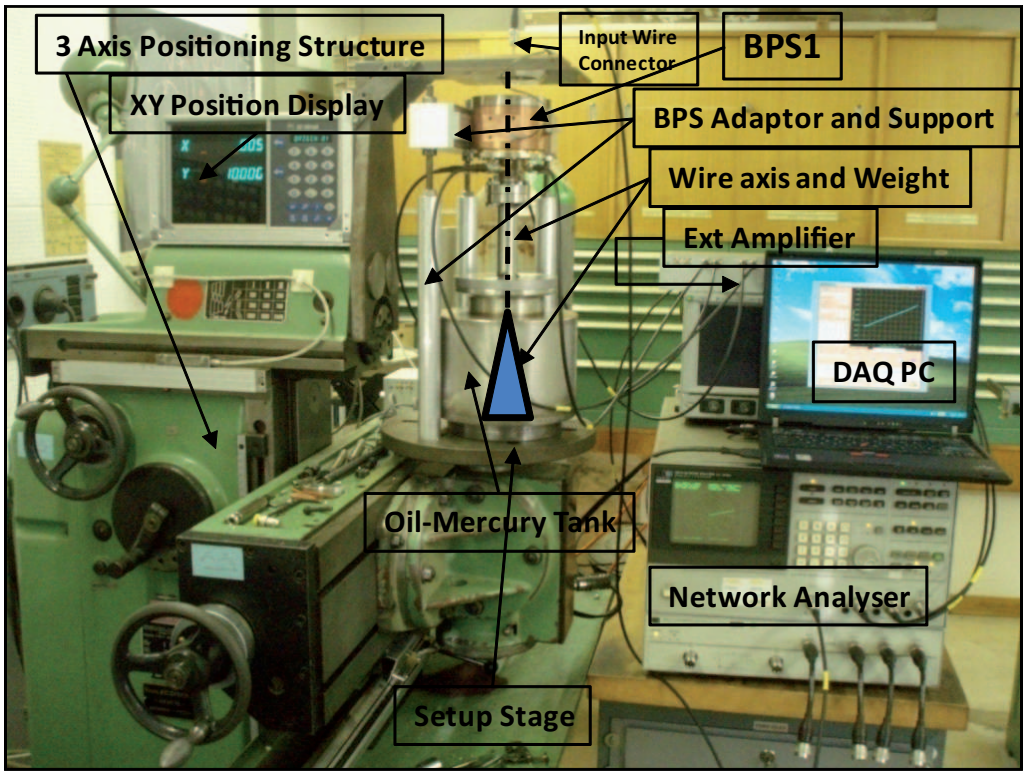

Figure 4.1: Testbench setup for wire test with the BPS installed (left side); BPS Amplifier connected to the four electrode signals: V_+, H_+, V_- and H_- (left side of PC); Network Analyzer to generate the excitation signal and capture the amplifier output signals: ΔV, ΔH and Σ (right-bottom side); and the PC running a LabVIEW acquisition program.

In the following section, the procedures for each kind of test measurements will be described, as well as the resulting characterization parameters and plots.

4.2 Sensitivity and linearity error test

.

Firstly, the purpose of this test is to obtain the sensitivity for the vertical and horizontal planes, $S_{V,H}$, from the linear fit equations (2.8) explained in the chapter 2, which gives the variation of the normalized difference signals, $\Delta V/\Sigma$ and $\Delta H/\Sigma$, with respect to the vertical and horizontal positions, respectively. Also, from the same measurements but for the linear fit relations (2.7), the deviation of the BPS1 center position measurement from the mechanical center, so called electric offsets for both planes, $EOS_{V,H}$ are obtained. In second place, the linearity errors for both planes are calculated, also from the linear fits data, having taken three points per wire position to be able to perform a first error analysis.

The wire was excited with a sinusoidal signal of 1 MHz, in the pass-band of the BPS1, and power amplitude of 0 dBm (1 mW), generated from a network analyzer. The four electrode outputs (V_+, H_+, V_-, H_-) were connected to a known and calibrated external amplifier, used in previous BPM developments, with linear gain factors of: $G_\Delta = 1.065$ and $G_\Sigma = 0.3477$, for the Δ and Σ channels. Then, the output amplifier signals (ΔV,

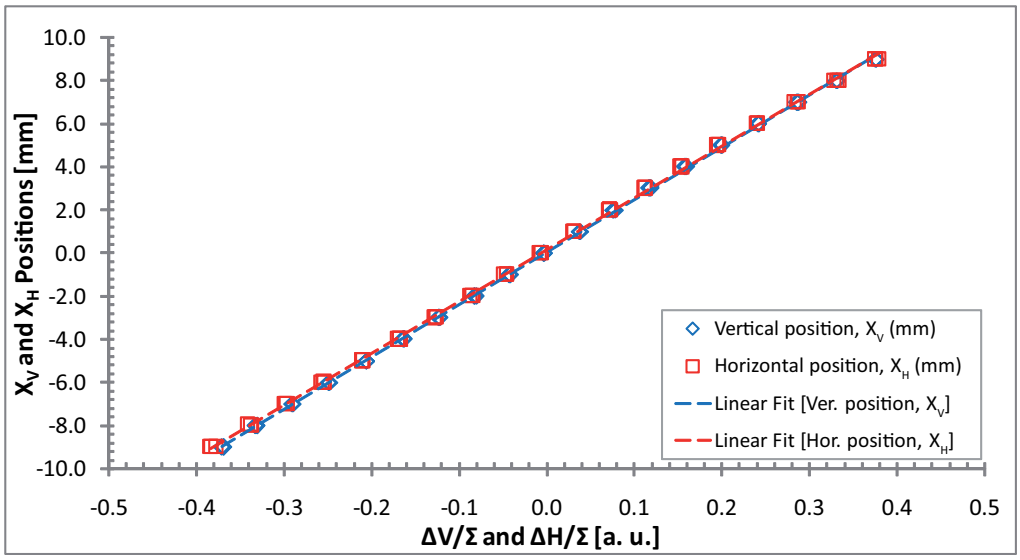

Figure 4.2: Measured data and linear fits to get the electric offsets, $EOS_{V,H}$, for the vertical and horizontal planes (3 sample measures per wire position and plane).

ΔH, and Σ) were driven to the network analyzer inputs where the difference signals were normalized to the sum signal, making them independent of the input signal amplitude (beam current). Moreover, the incoming signal amplitude was averaged with 16 samples to reduce the noise influence.

Finally, the measurements were taken with a PC running a LabVIEW program that acquired the wire position from the digital position encoder of the testbench positioning system; and the normalized signals, $\Delta V/\Sigma$ and $\Delta H/\Sigma$, from the network analyzer GPIB bus. These measures were taken for each plane independently, changing the wire position with respect to the BPS mechanical center calibrated previously.

One important remark about the final Δ/Σ measures is that they were divided automatically in the PC by the gain factors of the external amplifier channels in order to get just the BPS true output level without amplification. So, indeed, the role of the amplifier was only to mix the BPS electrode output signals to yield the desired difference and sum signals.

The electric offsets for the vertical and horizontal plane were obtained from the origin ordinate of the linear relations (2.7) fitted to the measured data of figure 4.2. Similarly, fitting the inverted linear relations (2.8) to the experimental data of the figure 4.3, we got the sensitivity for each plane from the respective slopes. Notice that these parameters were calculated for positions between ±9 mm, beyond the range of interest of ±5 mm specified in the table 2.1.

Therefore, when the beam is centered, the BPS1 electric offsets for both coordinate planes are:

- EOS_V=(0.03±0.01)mm, for the vertical plane;
- EOS_H=(0.15±0.02)mm, for the horizontal plane.

Likewise, the BPS1 sensitivity to the beam position displacements in both coordinate planes are:

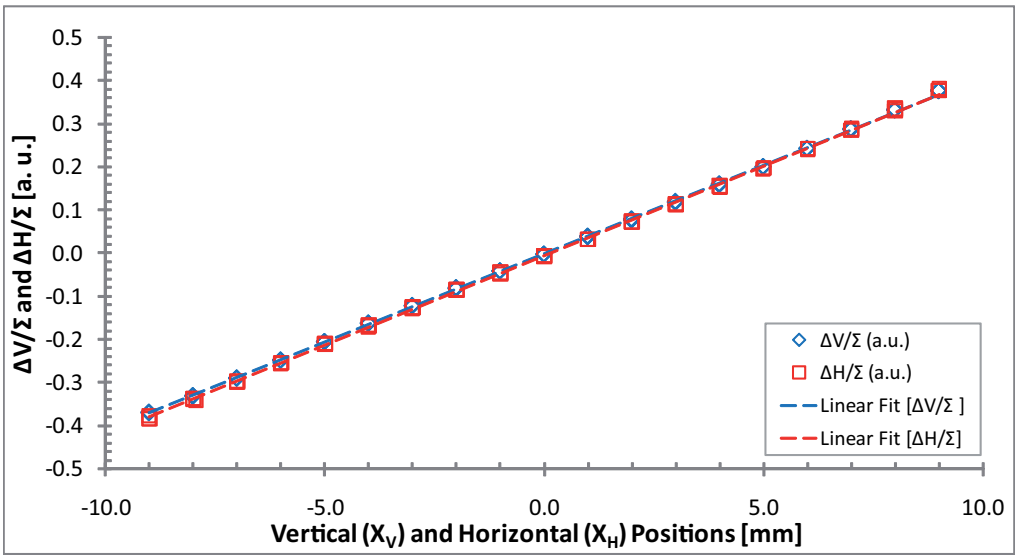

Figure 4.3: Measured data and linear fits to get the sensitivity parameters, $S_{V,H}$, as the linear fits slopes, for the vertical and horizontal planes (3 sample measures per wire position and plane).

- S_V=(41.09±0.08)10^{-3}mm^{-1}, for the vertical plane;
- S_H=(41.53±0.17)10^{-3}mm^{-1}, for the horizontal plane.

These BPS1 characteristic parameters will be used in the normal procedure to obtain the position from the sensitivity, and compensate the electric offsets by software in the control room servers. In principle, these parameters results were considered satisfactory for the correct performance of the BPS1 prototype.

At the end of subsection 2.2.2 was stated that the BPS1 performance is mainly determined by the overall precision (accuracy), σ_V and σ_H, for each coordinate plane. These characteristic parameters come from the linearity error analysis done for the data depicted in the linear fit plot of figure 4.3. Then, the linearity error was calculated for each position of both coordinate planes, as the deviation of the measured wire position from the linear fit represented by the relations (2.7), and the resulting plots are presented in the figure 4.4.

Furthermore, as it was previously discussed at the end of section 2.2.2, the linearity errors were obtained for the range of interest (±5 mm), and it was calculated the root mean square (RMS) linearity error, or variance, from the data depicted in the figure 4.4 of all the positions in the range of interest, yielding the BPS1 overall precision or accuracy:

- σ_V = 78 μm, for the vertical plane;
- σ_H = 170 μm, for the horizontal plane.

From the plots in the figure 4.4, jointly with the last accuracy results, we can observe that there is a significant difference between both coordinate planes. The horizontal plane shows higher error values for every position and, thus, an unacceptable increase in the horizontal accuracy parameter, σ_H. This can be justified by a misalignment of the primary electrodes from the real horizontal plane, what would increase the linearity errors for all

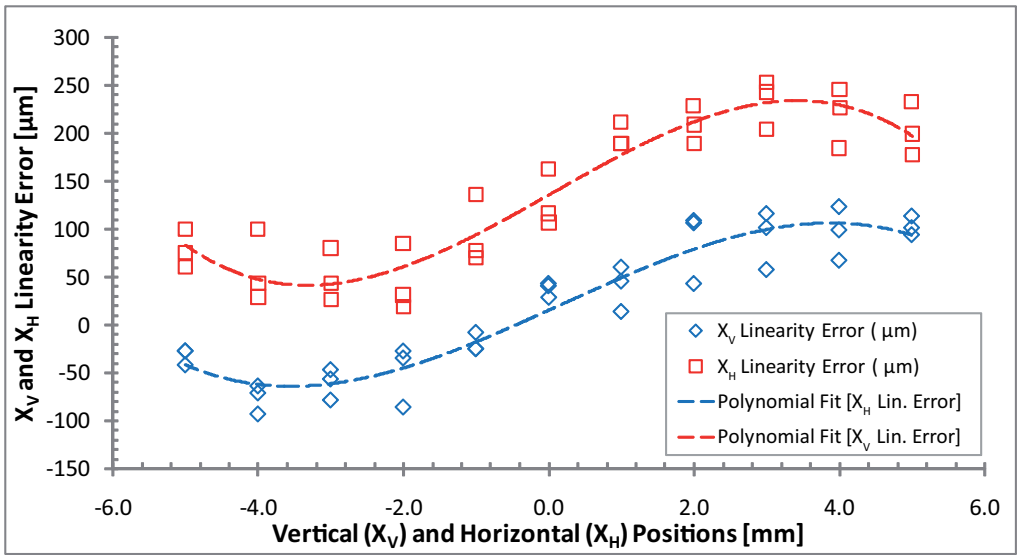

Figure 4.4: Linearity error for the vertical an horizontal plane wire positions (with 3 sample measures per wire position and plane).

the measured positions, but it would keep the typical s-shape of the plot. The horizontal plane misalignment causes will be revised and corrected in the series production of the BPS.

With respect to the TBL specifications for the BPS, the overall precision for both coordinate planes was found to be above the specified upper limit of 50 μm, so they must be lowered to accomplish the specifications. Apart from the misalignment in the horizontal plane, another reason for the poor values of the overall precision could be due to the low current intensity we could get in the wire, just only 13 mA, whereas the BPS1 is designed to manage a beam current of 30 A. This means, according to relation (3.5), a sum signal amplitude of, $\Sigma \approx 7$mV. In consequence, for these very low level amplitudes, a typical noise level of 1 mV could have a great influence in the position measures, increasing the linearity errors as a result. Concerning the test setup, it must be said that in spite of having higher currents at the input wire connector, the low current through the wire was caused by a resistor divider after the input connector of the testbench, which was used for matching purposes, and, presumably, for testing devices with different features. The low current influence in the BPS linearity errors and the way to improve the accuracy results will be investigated in a future work.

4.3 Frequency response test

.

The main aim of the frequency response test is to measure the low and high cut-off frequencies, described in the section 3.2.2, for two ways of exciting the BPS1 prototype: the wire and the calibration inputs (Cal+ and Cal−). Then, its associated droop and rise time constants, $\tau_{droop\Sigma}$, $\tau_{droop\Delta}$ and τ_{rise}, can be calculated from the relations (3.17), (3.18) and (3.19). In addition, this characteristic time constants can also be measured directly from a transmitted pulse signal, and, in this case, the cut-off frequencies would be calculated from the same relations.

Therefore, it was decided to measure the cut-off frequencies from the BPS1 frequency response using a Network Analyzer (NA), leading to more precise measurements of the cut-off frequencies due to its higher immunity to noise than a scope measuring time pulse signals. Moreover, in our particular case, having such a low current in the wire, we needed to improve the noisy frequency response of the BPS1 transfer magnitude captured by the NA, which is the ratio of the BPS1 output signals over the input or excitation signal. In order to get the BPS1 transfer ratio, the frequency sweep signal generated by the NA must be split in two equal signals, one for exciting the BPS1 input (wire or calibration), and the other one for getting the same BPS1 excitation signal at the NA reference input port. Then, with the BPS1 output signals connected to the NA, through its available signal input ports, the NA will be able to calculate the BPS1 transfer ratio from the signal ports over the reference port. In this way, the BPS1 frequency response could be cleaned just by attenuating only the reference signal at the NA, but not the signal used to excite the BPS1, increasing artificially the BPS1 transfer ratio in the NA.

The frequency span of the NA was set between 100 Hz and 200 MHz. And, it must be commented that, due to the problem of the low current in the wire, the relative power magnitude (in dB) between the BPS outputs and the reference signal at the NA was changed, in the way commented in the last paragraph, every time the BPS output power magnitude was too low to yield a clear response, improving the frequency response magnitude over the noise. Although, the variation of the relative power magnitude did not cause any problem, because the important parameters to be determined were the cut-off frequencies, and they are not affected by this fact.

In the next subsection, the frequency response plots for the BPS1 prototype will be presented, first for the case of wire input excitation at different positions; and, in second place, for the case of calibration inputs excitation. In both cases, getting the frequency response for the electrodes output signals (V_+, H_+, V_-, H_-), the difference signals for both planes (ΔV, ΔH), and the sum signal (Σ).

4.3.1 Frequency response results for the case of wire input excitation

.

From the figures 4.5 to 4.8 will be presented the frequency response plots for two wire excitation cases, when the wire is further from the center at +8 mm in both coordinate planes; and, for the centered wire position at 0 mm. These plots are enough representative in order to obtain the BPS1 characteristic cut-off frequencies, since they do not depend on the wire position, taking into account that for the Δ signals, and the wire in the central position, the frequency response will vanish showing only noise (figure 4.8). Also, remark

that the Σ frequency response will be constant for any wire position, since the Σ signal is the sum of all the electrode outputs and does not depend on the wire, or beam, position, as it was established in subsection 2.2.2.

Therefore, from the next representative plots we can obtain the BPS1 characteristic low cut-off frequencies, and its associated droop times, in the case of a wire (or beam) excitation:

- f_{L_Σ} = 1.76 kHz, is the low cut-off frequency for the electrode outputs and the Σ signal (eq. (3.15)); from here, τ_{droop_Σ} = 90 μs, is the droop time constant for the electrode outputs and the Σ signal (eq. (3.17));
- $f_{L_\Delta} \equiv f_{L_{\Delta V}} = f_{L_{\Delta H}}$ = 282 kHz, is the low cut-off frequency for the ΔV (vertical plane) and ΔH (horizontal plane) signals (eq. (3.16)); from here, $\tau_{droop_\Delta} \equiv \tau_{droop_{\Delta V}} = \tau_{droop_{\Delta H}}$ = 564 ns, is the droop time constant for the ΔV (vertical plane) and ΔH (horizontal plane) signals (eq. (3.18)).

Because the pulsed beam of TBL will have a maximum pulse period of t_{pulse} = 140 ns, the specification for the f_{L_Δ} is set to 10 kHz to get τ_{droop_Δ} = 16 μs (eq. (3.18)) and thus, as it was discussed at the end of section 2.2.4, the droop time constant for a Δ pulse would be much larger than its pulse period, being $\tau_{droop_\Delta}/t_{pulse} \simeq 10^2$, and allowing a good flat-top pulse transmission through the BPS outputs. In consequence, because for the BPS1 the measured f_{L_Δ} is clearly above the specified 10 kHz, it will need to be lowered, compensating the droop in the external amplifier Δ channels.

The high cut-off frequency could not be determined exactly due to signal reflections starting over 100 MHz, which was caused by the wire length (λ_{100MHz} = 3 m in the order of magnitude of the wire length), and a poor matching at its bottom end. In spite of this, one can say that:

- f_{high} > 100 MHz, for the high cut-off frequency of the electrode outputs, Δ and Σ signals (eq. (3.8)); from here, τ_{rise} <1.6 ns, for the rise time constant of the electrode outputs, Δ and Σ signals (eq. (3.19));

and, in consequence, the TBL specifications of table 2.1 are accomplished for the upper limit of the bandwidth.

4.3.2 Frequency response results for the case of calibration input excitation

.

From the figures 4.9 to 4.12 will be presented the frequency response plots for two calibration excitation cases, when exciting the positive calibration input (Cal+), which will be essentially equivalent to the negative one (Cal−); and, when exciting both calibration inputs at the same time (Cal+/−). This last case will be equivalent to the excitation case of a centered wire position.

Therefore, from the next representative plots can be measured the BPS1 characteristic low cut-off frequencies for the BPS calibration inputs, getting the same results as in the wire excitation case for the high cut-off frequencies. Then, the frequency response results for the calibration excitation case are summarized as follows:t-off frequencies. Then, the frequency response results for the calibration excitation case are summarized as follows:

- $f_{L_{\Sigma[Cal]}}$ = 1.76 kHz, is the low cut-off frequency for the electrode outputs and the Σ signal (eq. (3.15)); from here, $\tau_{droop_{\Sigma[Cal]}}$ = 90 μs, is the droop time constant for the electrode outputs and the Σ signal (eq. (3.17));

- $f_{L_{\Delta[Cal]}} \equiv f_{L_{\Delta V[Cal]}} = f_{L_{\Delta H[Cal]}}$ = 180 kHz, is the low cut-off frequency for the ΔV (vertical plane) and ΔH (horizontal plane) signals; from here, $\tau_{droop_{\Delta[Cal]}} \equiv \tau_{droop_{\Delta V[Cal]}} = \tau_{droop_{\Delta H[Cal]}}$ = 884 ns, is the droop time constant for the ΔV (vertical plane) and ΔH (horizontal plane) signals (eq. (3.18));

- $f_{high[Cal]} >$ 100 MHz, for the high cut-off frequency of the electrode outputs, Δ and Σ signals (eq. (3.8)); from here, $\tau_{rise[Cal]}$ <1.6 ns, for the rise time constant of the electrode outputs, Δ and Σ signals (eq. (3.19)).

It must be noticed that, $f_{L_{\Delta[Cal]}} < f_{L_\Delta}$ (eq. (3.16)), and their difference is about 100 kHz. This difference raises a problem for the amplifier compensation in the Δ channels, in order to decrease the Δ low cut-off frequency for the wire, f_{L_Δ}; just, because the same compensation designed for this frequency will be applied to the lower cut-off frequency when exciting the calibration inputs, $f_{L_{\Delta[Cal]}}$. In consequence, only one droop time constant could be compensated correctly, and the transmitted pulses would have different droop times. This significant difference between the wire and the calibration low cut-off frequencies for the Δ*signals* is a new observed effect, and it will need to be investigated in a future work.

4.4 Pulse response

.

In the figures 4.13 and 4.14 are presented the plots of the pulse response for a pulse excitation in the wire, and a pulse excitation in the positive calibration input. These plots are just to illustrate the transmitted pulse response of the BPS1, and, also, to show the observed difference between the droop time constants for Δ signals, $\tau_{droop_{\Delta[Cal]}}$ and τ_{droop_Δ}, when the calibration and the wire are excited by a pulse. Finally, remark that for a given positive input pulse, the turns winding orientation in the transformers was chosen to get an inverted polarity pulse, as it was specified for a TBL electron beam [11].

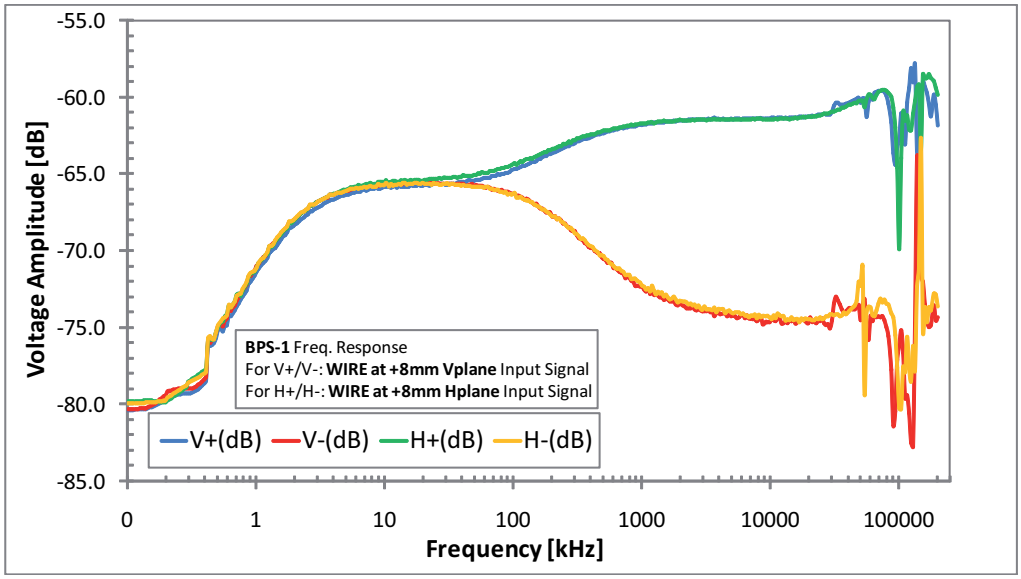

Figure 4.5: BPS1 frequency response for the electrode outputs at two different wire positions: +8 mm in the vertical plane (only V_+ and V_- are relevant); and, +8 mm in the horizontal plane (only H_+ and H_- are relevant).

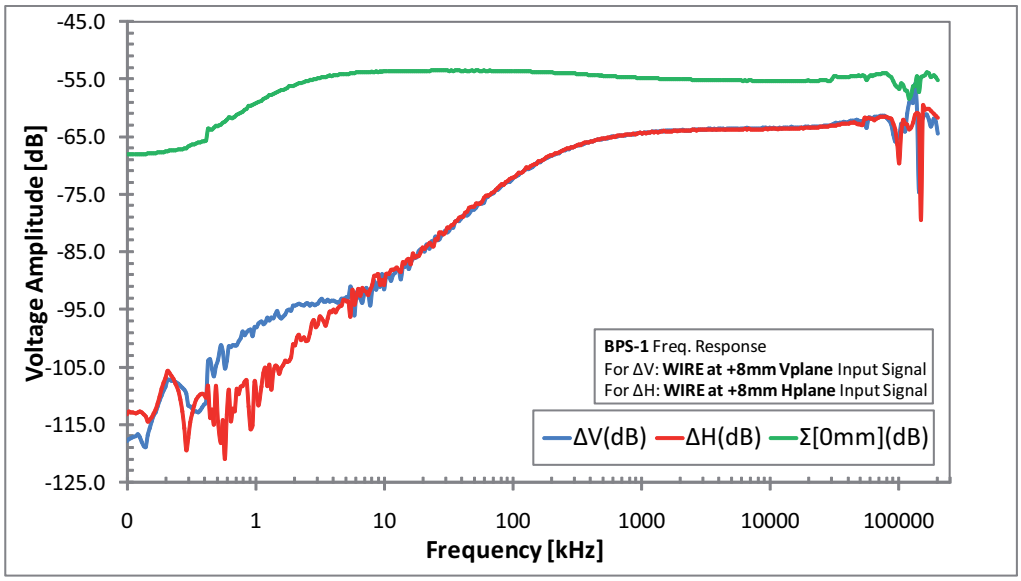

Figure 4.6: BPS1 frequency response for the Δ and Σ signals at two different wire positions: +8 mm in the vertical plane (only ΔV is relevant); and, +8 mm in the horizontal plane(only ΔH is relevant).

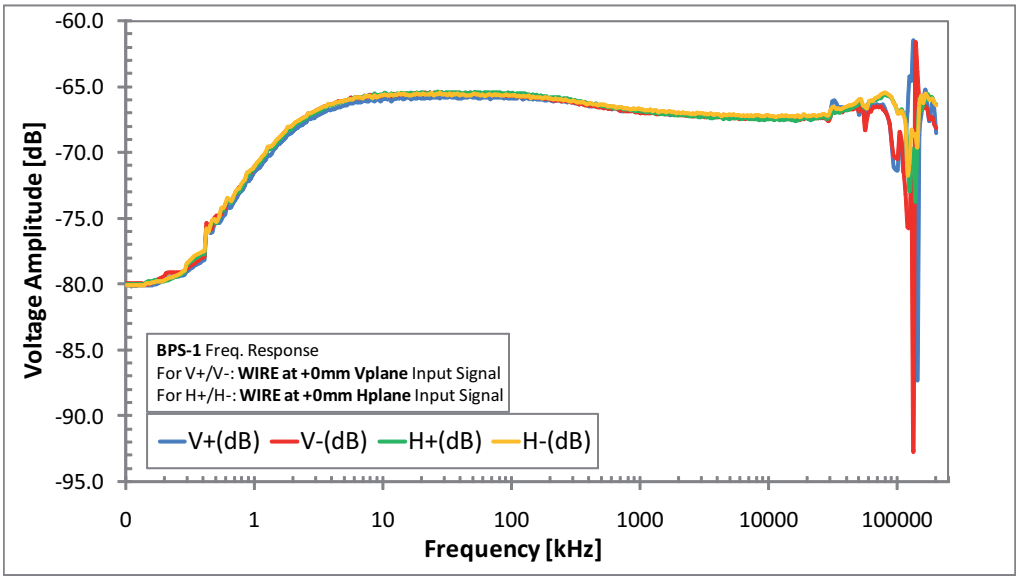

Figure 4.7: BPS1 frequency response for the electrode outputs at the centered wire position (0 mm).

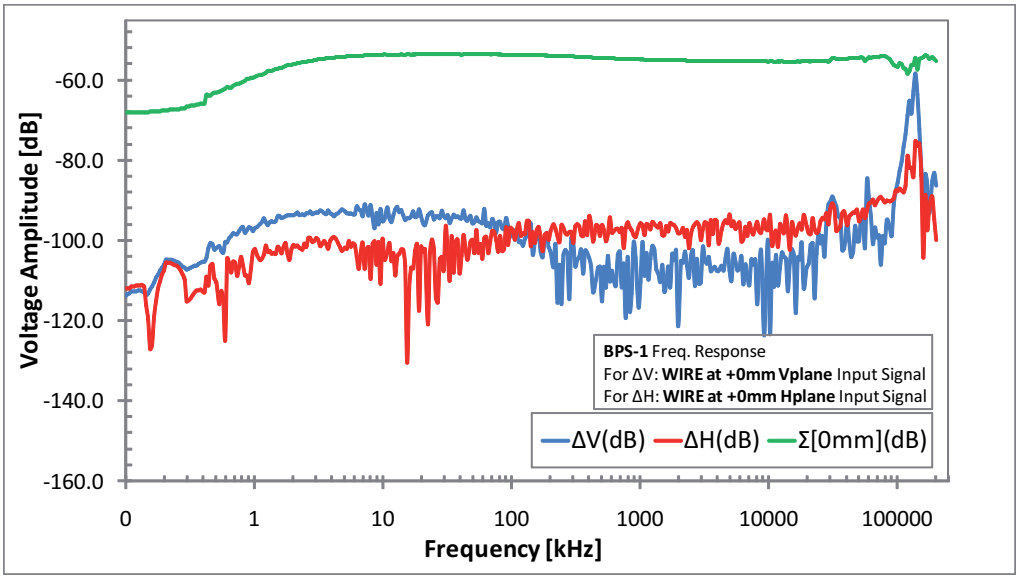

Figure 4.8: BPS1 frequency response for the Δ and Σ signals at the centered wire position (0 mm).

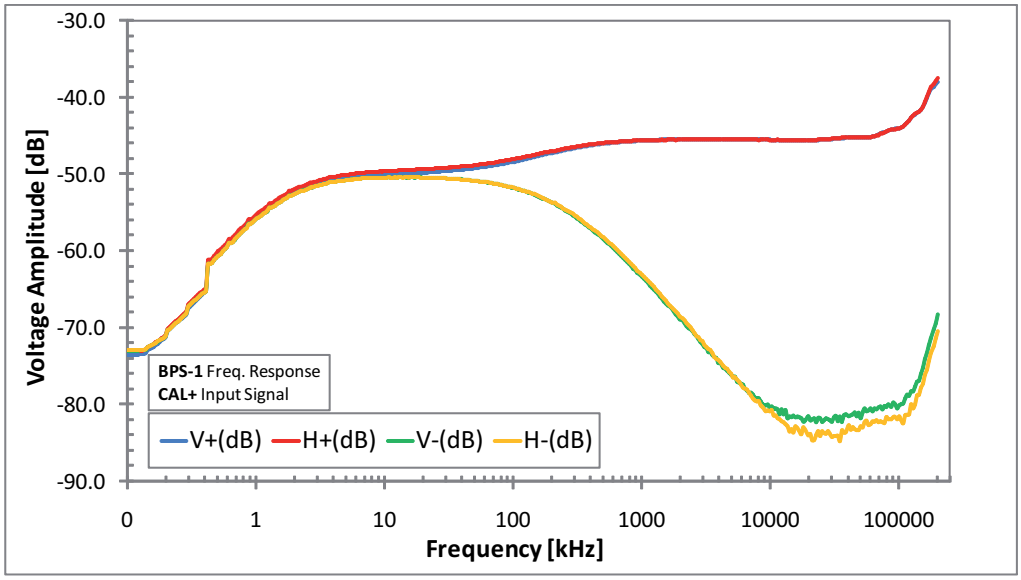

Figure 4.9: BPS1 frequency response for the electrode outputs of both planes when exciting the positive calibration input, Cal+.

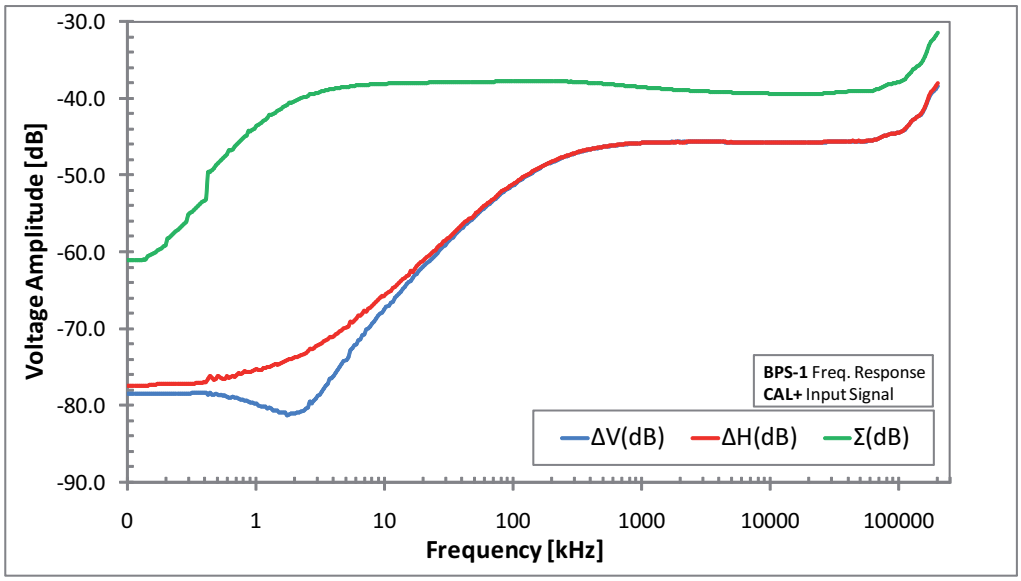

Figure 4.10: BPS1 frequency response for the ΔV, ΔH and Σ signals when exciting the positive calibration input, Cal+.

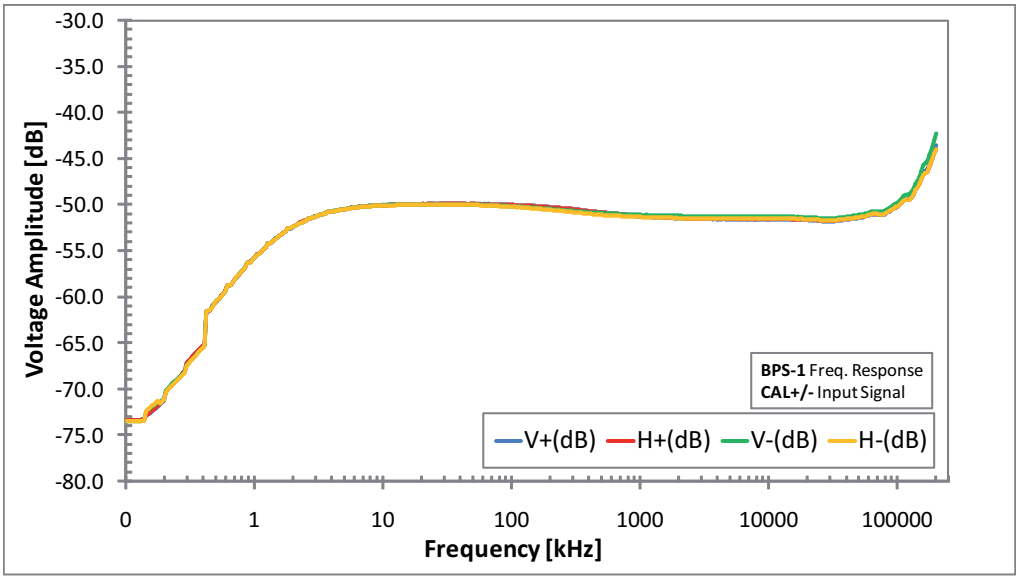

Figure 4.11: BPS1 frequency response for the electrode outputs of both planes when exciting the positive (Cal+) and negative (Cal−) calibration input at the same time.

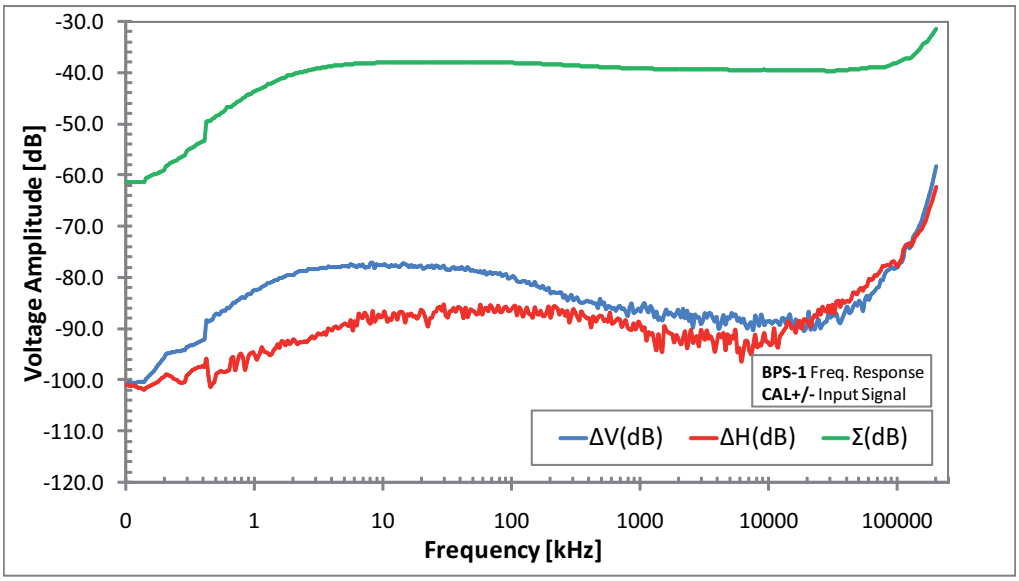

Figure 4.12: BPS1 frequency response for the ΔV, ΔH and Σ signals when exciting the positive (Cal+) and negative (Cal−) calibration input at the same time.

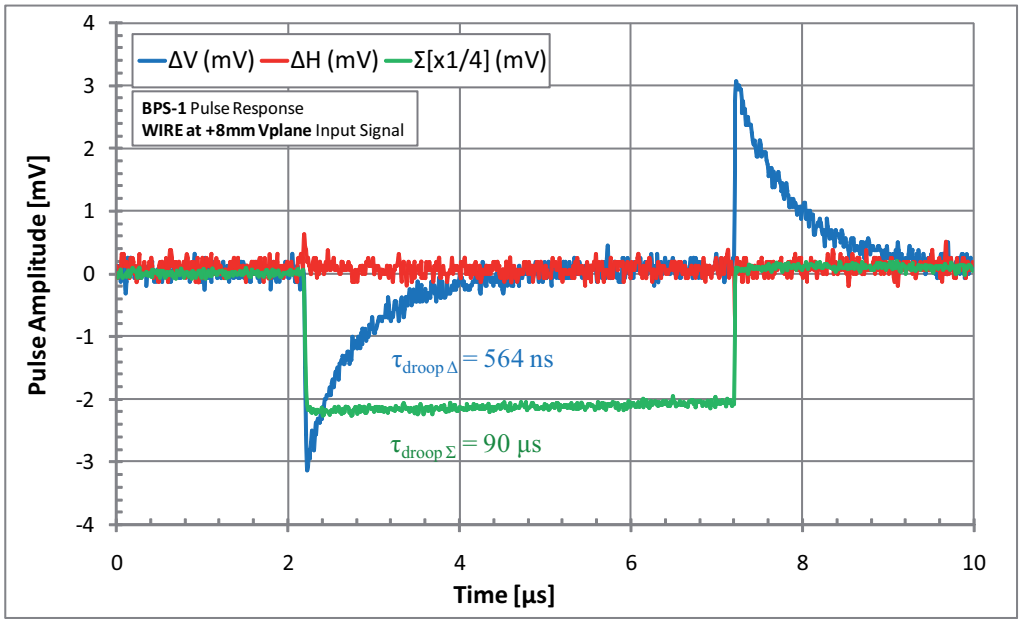

Figure 4.13: BPS1 transmitted pulse for Δ and Σ signals at +8 mm wire position in the vertical plane, and positive input pulse of 5 V and 5 μs.

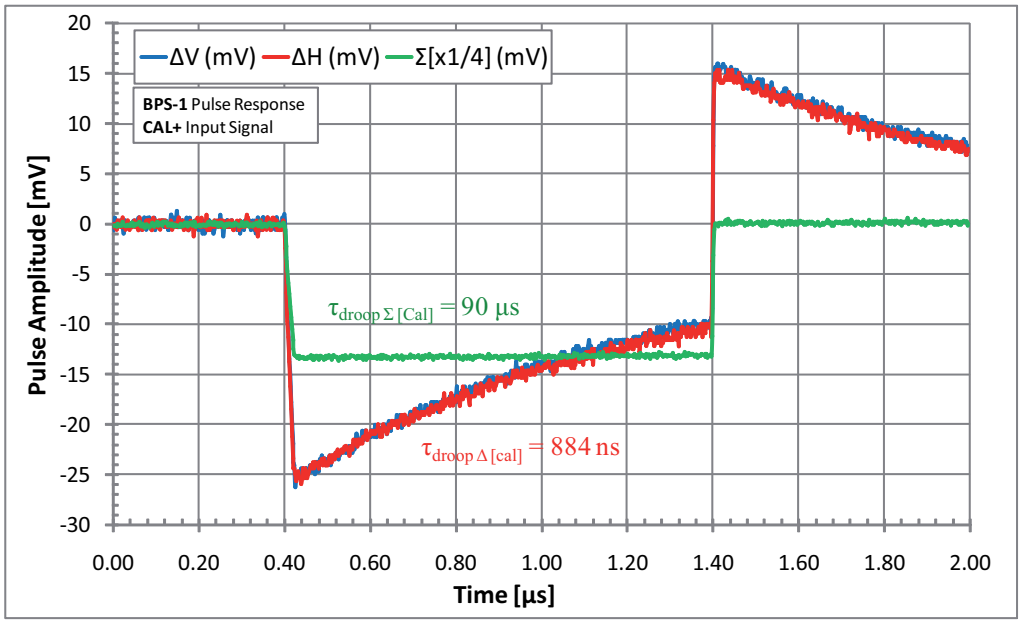

Figure 4.14: BPS1 transmitted pulse for Δ and Σ signals with positive calibration input excitation (Cal+), and positive input pulse of 5 V and 1 μs.

Chapter 5

Conclusions and Future Work

A set of two BPS prototypes with the associated electronics were designed and constructed. The electric model and characterization parameters: sensitivity, overall precision (accuracy), electrical offset and cut-off frequencies with its associated time constants; has been determined with the wire method test. The BPS1 performances are summarized in the table 5.1. The performed tests yield good linearity results and reasonably low electrical offsets from the mechanical center. Also, from the linearity errors analysis can be stated that the overall precision results have to be ameliorated, considering the effect of the very low excitation current in the wire and the misalignment for the horizontal plane electrodes. Concerning the frequency response measurements, the low cut-off frequencies for the Δ signals are equal for the vertical and horizontal planes, and they are given for performing the compensation of droop time constants with the external amplifier, but they show a difference of around 100 kHz between the low cut-off frequencies for the wire/beam and the calibration excitations. This effect never seen before must be investigated in a future work. The low cut-off frequencies for the Σ signals, corresponding also to each electrode output frequency response, are the same for both cases wire/beam and calibration excitation, and they are under specifications (below 10 kHz), as well as, the high cut-off frequency that we could determine to be above the required 100 MHz.

The construction of 15 BPS units for the whole TBL line, and their respective characterization tests, will start after finishing the characterization of BPS1 with a real beam. This second phase of our collaboration with the CTF3 project is proposed as future PhD work.

To carry out this work, a new improved setup will be built for testing the BPS' series. In the figure 5.1 it is shown a sketch of the proposed design for the new wire test setup. This testbench setup is inspired in the one at BI-PI group labs, and it will be used to perform the needed improvement tests in the BPS2 prototype unit, and for the characterization tests of the full BPS' series at IFIC. The main features of this new testbench setup is that the BPS under test will be moved by a motorized XY axis to change the relative wire position with respect to the BPS, and, moreover, the wire will be fed with a higher current to avoid the low current effects in the test measurements. The wire positioning system will allow to fully automatize the measures and, due to its high resolution (from 0.3 μm to 1 μm), we will also be able to determine, or, for a lower current than the beam nominal current, at least estimate the minimum position resolution down to 5 μm according to TBL specifications, with enough accuracy. The final design is under study and subsequent modifications will be done to improve this testbench setup.

BPS1 Sensitivity and Linearity Parameters	
Vertical Sensitivity, S_V	41.09 mm^{-1}
Horizontal Sensitivity, S_H	41.53 mm^{-1}
Vertical Electric Offset, EOS_V	0.03 mm
Horizontal Electric Offset, EOS_H	0.15 mm
Vertical overall precision (accuracy), σ_V	78 μm
Horizontal overall precision (accuracy), σ_H	170 μm
BPS1 Characteristic Output Levels	
Sum signal level, Σ	16.5 V
Difference signals max. levels, $\|\Delta V\|_{max}$, $\|\Delta H\|_{max}$	8.25 V
Centered beam level, $V_{sec}(x_V = 0, x_H = 0)$	4.125 V
BPS1 Frequency Response (Bandwidth) Parameters	
Σ low cut-off frequency, f_{L_Σ}	1.76 kHz
Δ low cut-off frequency, f_{L_Δ}	282 kHz
Σ[Cal] low cut-off frequency, $f_{L_{\Sigma[Cal]}}$	1.76 kHz
Δ[Cal] low cut-off frequency, $f_{L_{\Delta[Cal]}}$	180 kHz
High cut-off frequency, f_{high}	>100 MHz
High cut-off frequency calibration, $f_{high[Cal]}$	>100 MHz
BPS1 Pulse-Time Response Parameters	
Σ droop time constant, τ_{droop_Σ}	90 μs
Δ droop time constant, τ_{droop_Δ}	564 ns
Σ[Cal] droop time constant, $\tau_{droop_{\Sigma[Cal]}}$	90 μs
Δ[Cal] droop time constant, $\tau_{droop_{\Delta[Cal]}}$	884 ns
Rise time constant, τ_{rise}	<1.6 ns
Rise time constant calibration, $\tau_{rise[Cal]}$	<1.6 ns

Table 5.1: BPS1 monitor prototype performances.

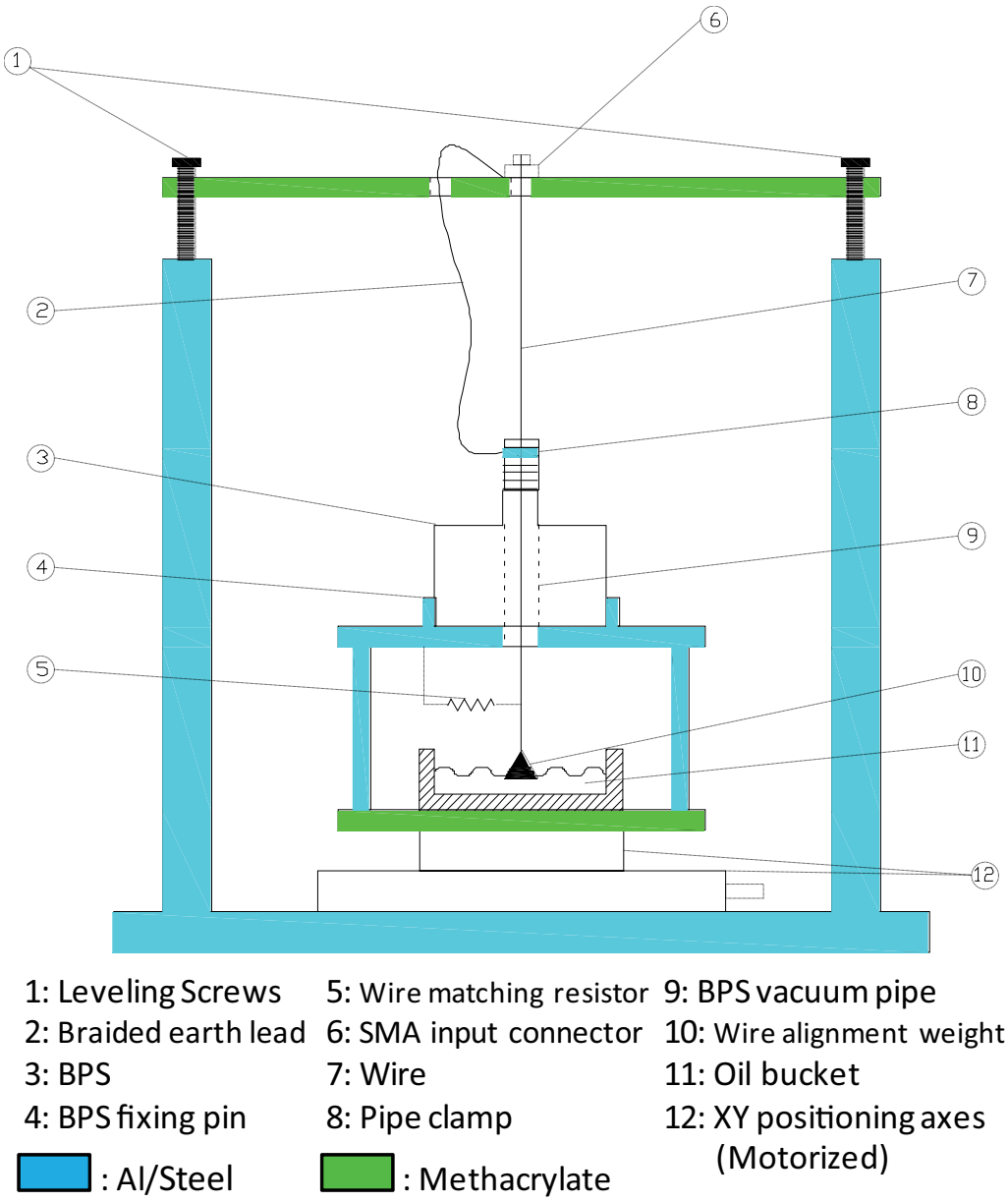

Figure 5.1: Sketch of the new wire test setup design with motorized XY positioning system to be build at IFIC (final design pending on further improvements).

Bibliography

[1] B. Barish, M. Ross, N. Walker, A. Yamamoto, *ILC Research and Development Plan for the Technical Design Phase*. ILC Global Design Effort, Release 2, June 2008.

[2] G. Guinard and The CLIC Study Team, *A 3 TeV e^+e^- Linear Collider based on CLIC Technology*. CERN 2000008, 28 July 2000, Proton Synchrotron Division.

[3] G. Geschonke, A. Ghigo et al., *CTF3 design report*, CERN/PS 2002-008 (RF). CTF3 Note 047, 2002.

[4] S. Döebert, D. Schulte, I. Syratchev, *Status report of the CTF3 Test Beam Line*. CTF3 Note 076, 2006.

[5] J.J. García-Garrigós, A. Faus-Golfe, J.V. Civera-Navarrete, *Design and Construction of an Inductive Pick-up for Beam Position Monitoring in the Test Beam Line of The CTF3*. Proceedings of the 11th European Particle Accelerator Conference EPAC'08, paper TUPC028, pages 1110-1112. JACoW conference proceedings.

[6] P. Forck, *Lecture Notes on Beam Instrumentation and Diagnostics*. Gesellschaft für Schwerionenforschung (GSI), Joint Universities Accelerator School (JUAS) 2007.

[7] H. Koziol, *Beam Diagnostics for Accelerators*. Page 154 in report CERN 2005-004, 2005.

[8] M. Gasior, *An inductive pick-up for beam position and current measurement*. CERN-AB-2003-053-BDI.

[9] I. Podadera, S. Calatroni, L. Søby, *Precision Beam Position Monitor for EUROTeV*. EUROTEV Report 2007-046.

[10] R.E. Shafer, *Beam position monitoring*. In S.R. Smith, editor, 7th Beam Instrumentation Workshop, volume 390, pages 2658. AIP Conference Proceedings, 1990.

[11] S. Döebert. Private communications.

[12] M. Gasior, *Hardware of the CTF3 beam position measurement system*. CTF3 Note 053, 2003.

[13] G. Montoro. Private communications.

[14] *VITROVAC - Amorphous Tape-Wound Cores for Digital Interface Transformers and Common Mode Chokes in ISDN - Equipment and Communication Systems*. Part number T60009-E4006-W650. Manufacturer VACUUMSCHMELZE GMBH & Co. KG, P.O. Box 2253, D-63412 Hanau, Germany.

[15] L. Søby and F. Guillot. Private communications.